ELECTRON PARAMAGNETIC RESONANCE AND OPTICAL STUDIES OF CRYSTALLINE SILICON DIOXIDE

By

BENJAMIN MARK ZAPATA

Bachelor of Science

The University of Texas at San Antonio

San Antonio, Texas

1987

Submitted to the Faculty of the
Graduate College of the
Oklahoma State University
in partial fulfillment of
the requirements for
the Degree of
MASTER OF SCIENCE
December, 1990

ELECTRON PARAMAGNETIC RESONANCE AND

OPTICAL STUDIES OF CRYSTALLINE

SILICON-DIOXIDE

Thesis Approved:

Larry E. Halliburton

Thesis Advisor

Joel J. Martin

James P. Wicksted

Norman N. Durham

Dean of the Graduate College

ACKNOWLEDGEMENTS

I express my appreciation towards Professor L. E. Halliburton who served as my thesis advisor. This project would not have been completed without his enthusiasm, guidance, and support.

My appreciation is also extended to Dr. J. J. Martin and Dr. J. Wicksted for their services on my thesis committee. In addition, my thanks goes out to Michael Scripsick (PhD.) for teaching me how to operate the Magnetic Resonance Laboratory. Moreover, my gratitude is also extended to Dr. Ching-Yuan Chen (whom I never met) for providing me with a dissertation to follow and, last but not least, my thanks is also extended to Dr. Gary Edwards for his humor and cooling block design.

I also wish to thank my wife, Cindy, and my son, David, for their love and support throughout this trying time of my life. I am also grateful to God for watching over me and my family.

TABLE OF CONTENTS

LIST OF TABLES

LIST OF FIGURES

CHAPTER I

INTRODUCTION

Background

The research described in this thesis is concerned with the characterization of point defects in silicon dioxide, or as it is commonly known, quartz.

Quartz is a material that is easily found in nature. Large deposits occur in areas such as Alaska, Arkansas, and Brazil. However, due to the higher concentration of impurities and the need to "select" untwinned crystals, natural quartz has been replaced by commercially grown synthetic quartz in nearly every application.

Synthetic quartz is grown hydrothermally. This method involves a pressure vessel called an autoclave. The autoclave contains one or more seed crystals held above a natural quartz nutrient. The vessel is then filled with water and mineralizers such as sodium hydroxide (NaOH) or sodium carbonate (Na_2CO_3) to help dissolve the nutrient. After filling, the vessel is sealed and heated to a temperature near $350^{o}C$. The resulting pressure is 2000 atms. A thermal gradient, maintained between the seed and the nutrient, produces a thermal circulation. The thermal circulation causes the elements from the solution to be deposited onto

the seed, thus "growing" a crystal. Impurities contained in the crystal can come from the nutrient, mineralizers, seed, or vessel wall [1].

The usual impurities contained in synthetic quartz are aluminum, sodium, lithium, hydrogen, and iron. The concentrations of these impurities often are at the parts-per-million level and ,recently, some growers have shown that these impurities can be reduced to the parts-per-billion level. The concentrations of impurities in synthetic quartz is at least an order of magnitude lower than in natural quartz [2].

Synthetic quartz has found application in a variety of frequency control devices, including precision resonators, narrow band filters, and surface acoustic wave (SAW) devices [3]. The main reason quartz is so widely used is that it exhibits a phenomenon called piezoelectricity.

The piezoelectric effect occurs when lower symmetry crystals are compressed in a specific direction, thus producing a charge on their surface. When the pressure is released the charge disappears. More specifically, piezoelectricity is the electric polarization induced by mechanical strain in certain crystals [4]. This phenomena can be better explained by describing how a quartz oscillator works.

A quartz oscillator, for example, can resemble a bar with electrodes attached to it at opposite ends and which exhibits longitudinal modes of vibration. When an electric

field is applied, a converse piezoelectric effect will occur causing a mechanical strain in the crystal. When the electric field is removed, the crystal will mechanically relax to its equilibrium point and overshoot in the negative direction. At this point it will induce a voltage opposite in sign to that originally applied. The bar will continue to mechanically oscillate about its equilibrium point inducing alternating voltages. The alternating voltages have the same frequency as the mechanical oscillations. Of the two types of quartz, alpha and beta, alpha-quartz exhibits piezoelectricity and is used in oscillators.

Alpha-quartz is also known as low quartz because it only exists below a temperature of $573^{o}C$. It has trigonal crystal symmetry and belongs to point group 32. The Z axis (sometimes referred to as the c or optic axis) has threefold symmetry. There are three equivalent twofold axes separated by 120^{o} that lie in the plane perpendicular to the optic axis. The basic structure consists of interlinking slightly distorted SiO_4 tetrahedra with two types of Si-O bonds, one long and one short, as shown in figure 1 [3]. Alpha-quartz has large c-axis channels which allow interstitial ions to migrate along the channel and become trapped near substitutional impurities or point defects. In addition, alpha-quartz is neither completely ionic or covalent and has a wide band gap of 9 eV [5].

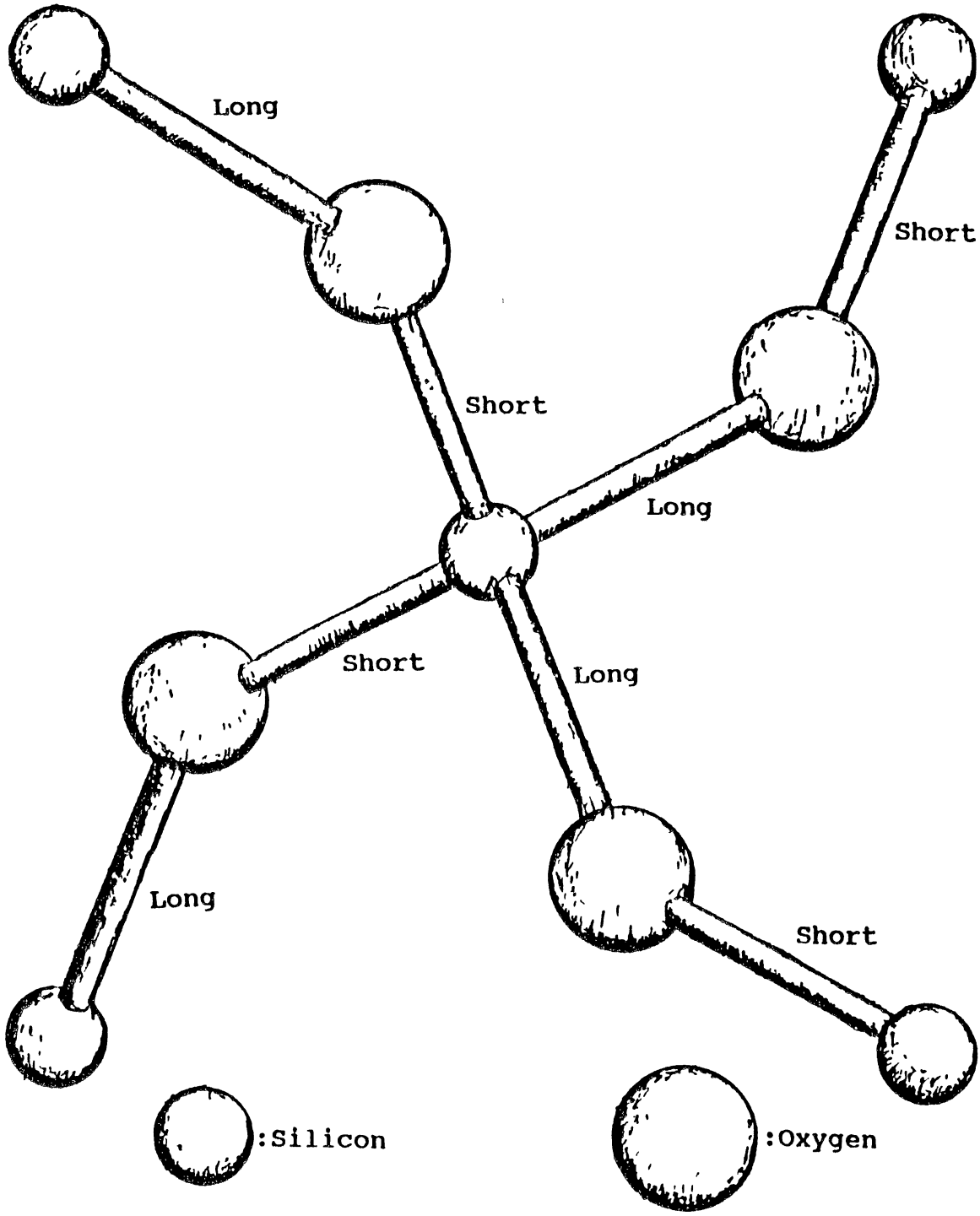

Figure 1. Crystal structure of quartz showing the long and short bonds

Defects in Quartz

Aluminum-Associated Centers

Aluminum ions easily substitute for silicon and require charge compensators (i.e., an Al^{3+} ion needs an additional positive-charged ion to compensate for the replaced Si^{4+} ion). Among the possible charge compensators for aluminum are H^+, Li^+, and Na^+ ions at interstitial sites and holes (i.e., an absent electron) at oxygen ions. These charge compensators are located next to a substitutional aluminum ion and give rise to either $[AlO_4/H^+]^o$, $[AlO_4/Li^+]^o$, $[AlO_4/Na^+]^o$, or $[AlO_4]^o$ defect centers. Notations for such centers were proposed by Weil [6]. Schematic representations of these aluminum-associated centers are given in figure 2.

In figure 2(a) the $[AlO_4/H^+]^o$ center consists of an interstitial proton bonded to an oxygen ion forming an OH^- molecule. The OH^- molecule is adjacent to the substitutional aluminum and gives rise to infrared absorption due to its stretching vibrations.

In figure 2(b) the $[AlO_4/M^+]^o$ center consists of an aluminum ion and an interstitial alkali next to it in the c-axis channel. M^+ can represents either Li^+ or Na^+ ions. This defect gives rise to one or more acoustic loss peaks because of the stress-induced motion of the alkali ion from one equilibrium position to another about the aluminum ion.

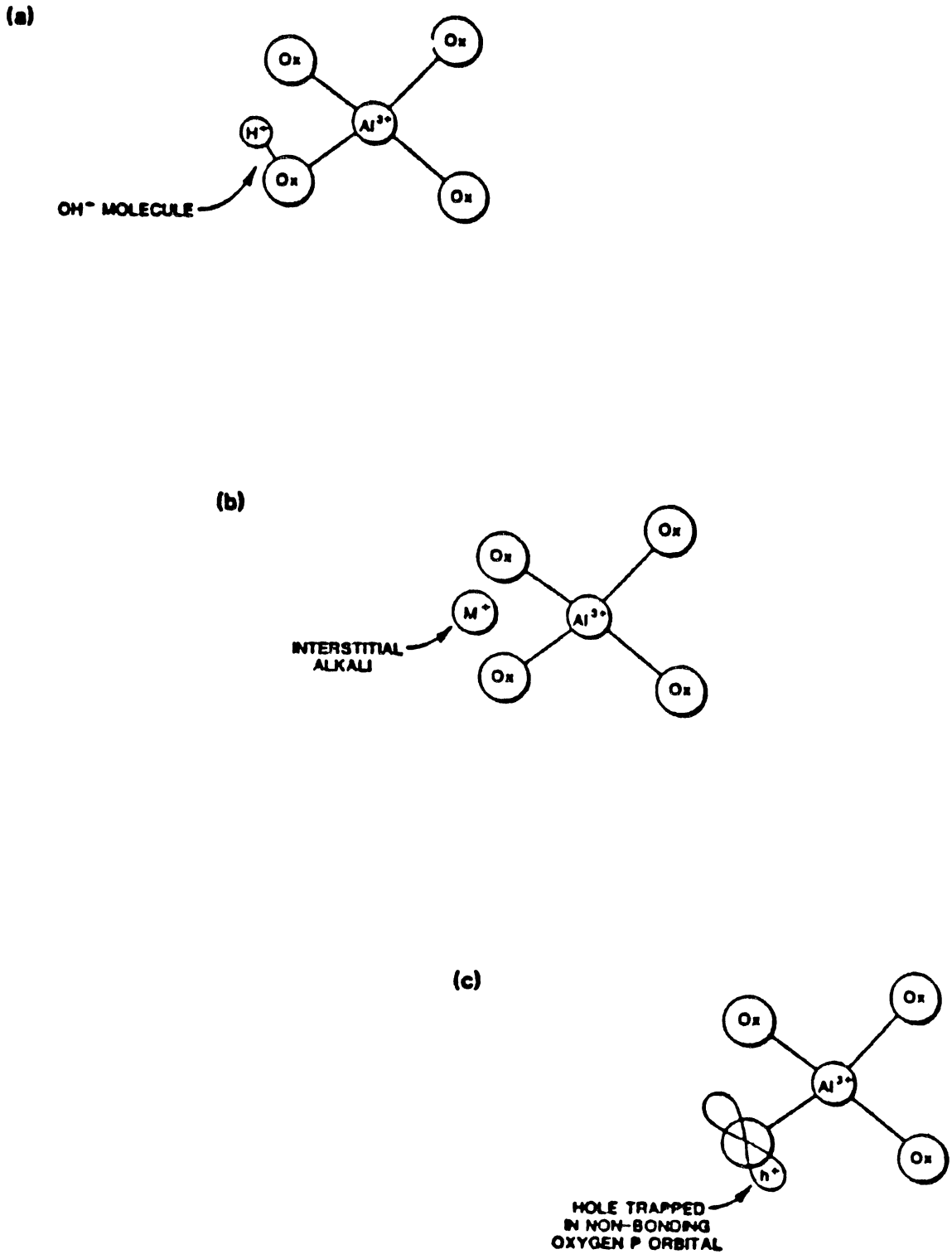

Figure 2. Models of Aluminum-Associated defects

Acoustic loss peaks related to Na^+ have been reported by King [5] and Martin [7]. Furthermore, dielectric loss is related to $[AlO_4/Na^+]^o$ centers as reported by Nowick et al. [8] and Stevels et al. [9].

Figure 2(c) shows a $[AlO_4]^o$ (i.e., aluminum hole) center which is a hole trapped in a non-bonding p orbital of an oxygen ion located next to a substitutional aluminum. Formation of an aluminum-hole center leaves an unpaired electron on the oxygen. The presence of these centers can be detected by electron paramagnetic resonance (EPR) at 77 K because of the unpaired electron [1].

Additional defects, similar to the aluminum-hole center, are formed when an aluminum ion next to an interstitial ion (Na^+, Li^+, or H^+) traps a radiation-induced hole. These are denoted $[AlO_4/M^+]^+$. These centers have two charge compensators for the aluminum and are positive charged. Nuttal et al. [10] have characterized the H^+ and Li^+ aluminum-hole centers using EPR. Moreover, Nuttal et al. [11] have characterized a variant form of this type of center which is the same except it has no neighboring interstitial ion and has trapped two radiation-induced holes. This is denoted as the $[AlO_4]^+$ center.

Oxygen-Vacancy Centers

The oxygen-vacancy-associated family of defects are referred to as E centers where E_1', E_2', E_4', E_1'', E_2'', and E_3'' are the commonly used notations. The superscript

single prime denotes one unpaired electron (S = 1/2) and the superscript double prime denotes two unpaired electrons (S = 1). The subscripts indicate various centers with the same spin. Most of the known information about these defects has come from EPR investigations. The EPR spectra of these centers exhibit narrow line widths (less than 0.1 G), g values slightly less than 2.0023, and long spin-lattice-relaxation times [1].

The E_1' center is a radiation-induced defect which was first reported by Weeks [12,13]. Weeks suggested, based on the observed long spin-lattice-relaxation times, that the center was an electron trapped at a silicon ion located between two oxygen vacancies. Silsbee [14] took a complete set of angular dependence data and determined a set of spin-Hamiltonian parameters for the g tensor, one strong hyperfine, and two weak hyperfine matrices. He then concluded that the E_1' center was an electron localized primarily on a silicon giving rise to the strong hyperfine (400 G splitting) and weakly interacting with two additional silicons giving rise to the two weak hyperfine (8 G and 9 G splitting). Theoretical studies by Feigl et al. [15] and Yip and Fowler [16] suggested that the center was an oxygen vacancy with an unpaired electron located in a non-bonding sp^3 hybrid orbital centered on one of the two neighboring silicons. There is a highly asymmetric relaxation of the two neighboring silicon atoms because one silicon, with the extra electron, moves toward the vacancy while the other

moves away. The EPR spectra and the proposed model by Yip and Fowler are shown in figure 3.

The E_2' center was first reported by Weeks and Nelson [13]. Its primary EPR spectrum consists of a doublet split by 0.4 G when the c axis is parallel to the magnetic field. There are two additional much less intense pairs of lines with a separation of 412 G. One pair is 193.5 G above the center doublet and the other is 218.5 G below. The separation within these pairs of lines is the same as the central 0.4-G-split doublet. The intensities of these outer lines is forty times less than the primary doublet which suggests that they arise from the hyperfine interaction of the trapped electron with a ^{29}Si nucleus. It was concluded by Weeks that the E_2' center was a Si-O divacancy with an electron trapped on a silicon ion adjacent to the oxygen vacancy with a proton trapped nearby. Jani [17] did a full angular dependence and spin-Hamiltonian parameter calculation on the two outer pairs of lines but he did not offer a definitive model.

Recently, Rudra et al. [18] tested a model for the E_2' center by means of a semiempirical molecular-orbital calculation. It was suggested that the E_2' center is a variant of the E_4' center (a hydrogen atom substituted for an oxygen atom) with one silicon neighbor relaxed outward, into a "bonded interstitial" position. The EPR spectrum and model proposed by Rudra [18] are shown in figure 4.

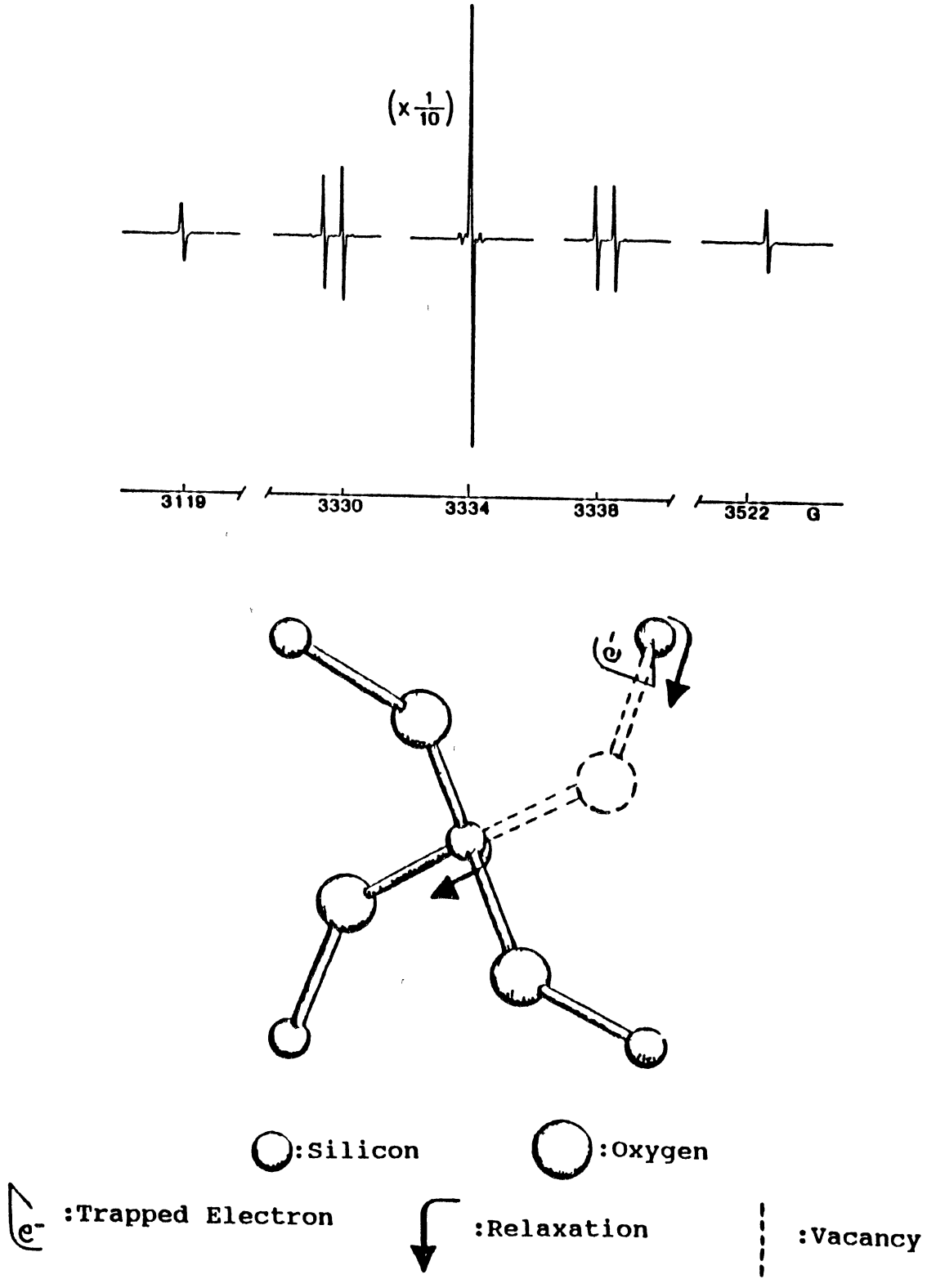

Figure 3. EPR spectrum and proposed model of the E_1' center. Data taken at 300 K with magnetic field parallel to c-axis and microwave frequency of 9.3358 GHz

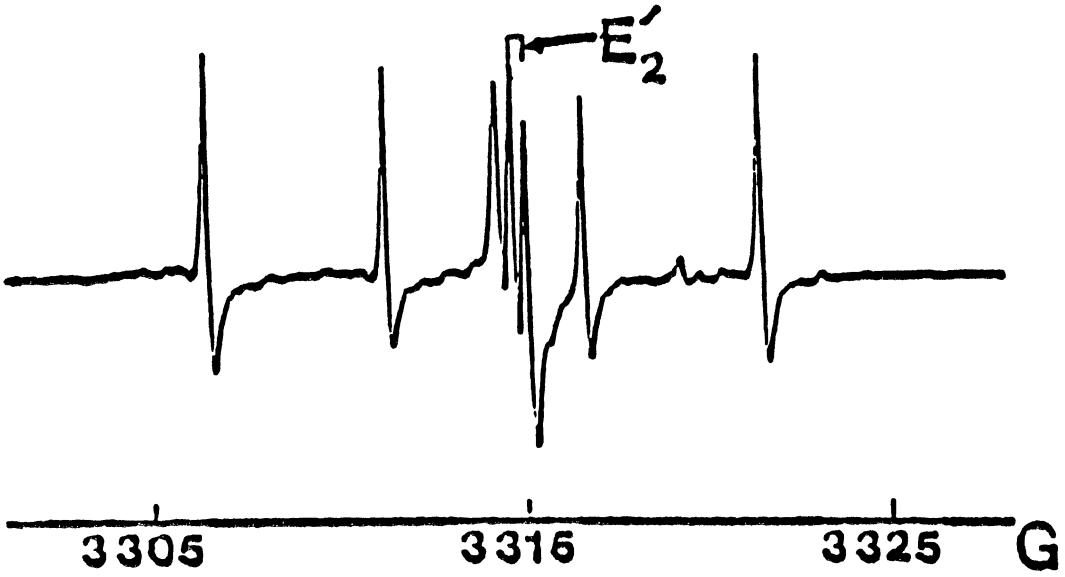

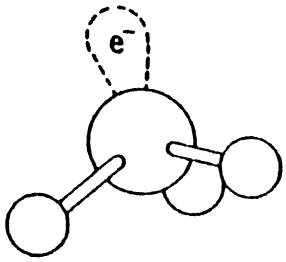

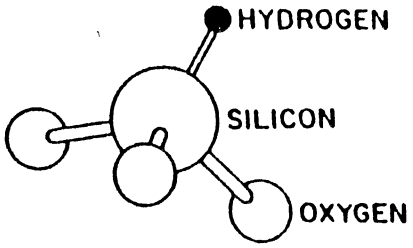

Figure 4. EPR spectrum and proposed model of the E_2' center. Data taken at 300 K with magnetic field parallel to c-axis and microwave frequency of 9.085 GHz

The E_4' center is similar to the E_1' center except it shows a hyperfine pattern from a 100% abundant nucleus. Weeks and Nelson [13] first reported this defect. It was found that the EPR spectrum at 9.1 GHz consisted of four lines with nearly equal spacing (4.8 G) and with nearly equal intensities. It was suggested that a 100% abundant I = 3/2 nucleus was the origin of the splitting since there were (2I+1) lines in the hyperfine pattern.

Further studies were done by Halliburton et al. [19]. At 20 GHz, it was noted that the separation of the inner pair of lines decreased while their intensities increased and that the intensities of the outer pair of lines decreased. At the higher microwave frequency, the outer pair of lines separated to 10.52 G which is close to the Larmor frequency for a proton. Thus, it was concluded that the E_4' center has S = 1/2 and the hyperfine structure comes from inter- actions with a proton I = 1/2 in a situation permitting observation of all $2S(2I+1)^2$ possible EPR transitions.

Isoya et al. [20] calculated the spin-Hamiltonian parameters and proposed a model for the E_4' center that consisted of an oxygen vacancy between two silicon ions with a hydride ion bonded to one of the two silicons. This model was supported, in good agreement with experimental data, by a detailed theoretical <u>ab initio</u> SCF-MO (Gaussian 70) calculation for a 15-atom cluster. The proposed model and EPR spectra are shown in figure 5.

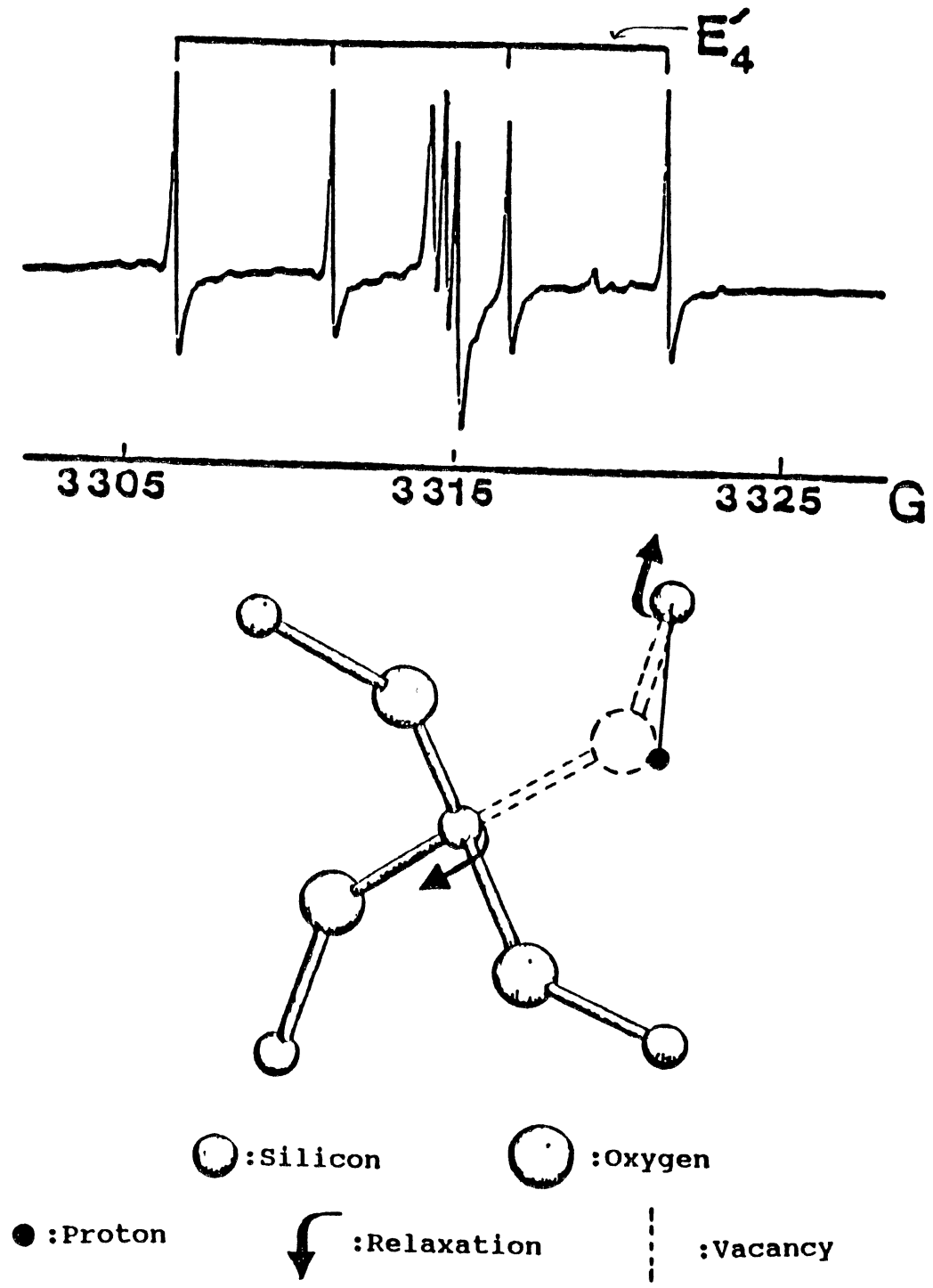

Figure 5. EPR spectrum and proposed model of the E_4' center. Data taken at 300 K with magnetic field parallel to c-axis and microwave frequency of 9.085 GHz

The E'' centers were first reported by Weeks and Abraham [21]. They suggested these were S = 1 states resulting from a dipole-dipole interaction of two nearby electrons in S = 1/2 states. A thorough EPR angular dependence and thermal anneal was done by Bossoli et al. [22] and it was concluded that the system was indeed a spin S = 1 because of a large angular dependence. It was then suggested that the E_1'' center consists of two oxygen vacancies with each having an adjacent unpaired electron (i.e., two neighboring E_1' centers). This suggestion is supported by the fact that there are two strong ^{29}Si hyperfine interactions for each E'' center. Furthermore, Jani [23] expanded this model by suggesting that there was a silicon vacancy as well and that the electrons were trapped in the sp^3 hybrid orbitals. The EPR spectra of the E'' centers and the general model of the E_1'' center proposed by Jani [23] can be seen in figure 6.

Hydrogen-Related Centers

Hydrogen is found in all quartz and gives rise to defects that are difficult to characterize. In high quality quartz most of the hydrogen is in the form of OH^- molecules. Thus, most of the research on hydrogen-related centers has utilized infrared absorption. However, ionizing radiation and thermal energy can release the proton from the molecule which, in turn, produces a hydrogen-related defect. Most of these latter defects are paramagnetic and observable with

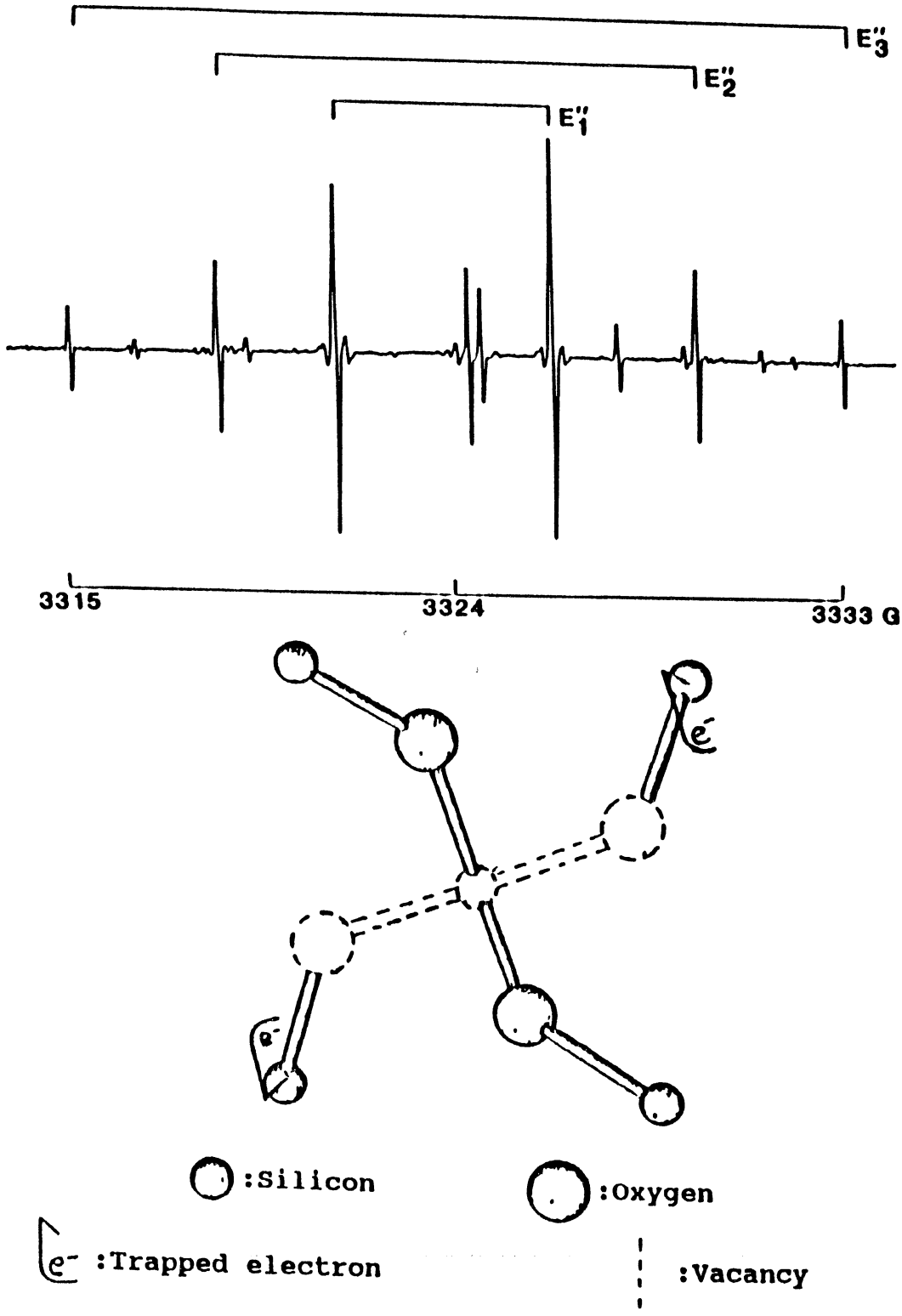

Figure 6. EPR spectra of E'' centers and proposed model for E_1'' center. Data taken at 300 K with magnetic field parallel to c-axis and microwave frequency of 9.3092 GHz

EPR. The first of these to be studied were the hydrogen atom, the E_2', and the E_4' centers [1]. Their EPR lines are very narrow and this associated high resolution has been invaluable in characterizing such defects.

The EPR spectrum of the hydrogen-atom center was first reported by Weeks and Abraham [24] and later investigations were reported by Perlson and Weil [25] and Isoya et al. [26]. This defect is a hydrogen atom and is produced by ionizing radiation at 77 K. It is thought that the irradiation leads to dissociation of the OH^- molecule followed by the displacement of the hydrogen. The atom then becomes trapped at an interstitial site and remains there as long as the temperature is below 125 K. The c-axis spectrum consists of a 520 G doublet due to the hyperfine interaction with the proton. This spectrum can be saturated with microwave power (i.e., has a long spin-lattice relaxation time) and the lines are 0.05 G wide.

Nuttal and Weil [27] reported another set of hydrogen related defects. These were formed by ionizing radiation and are holelike. One of the defects is thought to be a hole trapped at an oxygen ion next to a silicon vacancy containing four protons. Another defect, similar in nature, has only three protons in the silicon vacancy.

Chen [28] furthered our knowledge of paramagnetic hydrogen-related defects by doing complete defect production studies, thermal anneals, and angular dependences. He observed and characterized three new defects, which he

labeled H-1, H-2, and H-3. Specifically, the H-1 and H-2 centers exhibit saturation of their production curves beyond 100 Mrads of irradiation, they are holelike because of a positive g shift, they contained a single proton, and they have rapid reorientations of holes or ions because of short spin-lattice relaxation times. Therefore, the suggested precursor models consist of a silicon-oxygen divacancy with two protons bonded to adjacent oxygen ions. After a lengthy 77-K irradiation, one of the two protons has been replaced by a hole. The silicon-oxygen divacancy model is based largely on the fact that this type of defect is one of the few that can simultaneously trap a hole and a proton. To date, a model for the H-3 has not been proposed. The EPR spectra of the H-1, H-2, H-3, and $[H_3O_4]^o$ centers as well as the model for the H-1 and H-2 centers suggested by Chen [28] can be seen in figure 7.

Another set of hydrogen-related centers known as U-centers were first reported by Markes and Halliburton [29]. Collectively, these centers are denoted U-1, U-2, U-3, and U-4. The U-1 center appears "in-phase" and has a holelike g value with a S = 1/2 spin system and no hyperfine lines. The U-2 and U-3 centers appear "out-of-phase" and have electronlike g values and their doublet nature suggests a hyperfine interaction with a 100% abundant I = 1/2 nucleus, presumably hydrogen. In comparing the U-2 and U-3 centers to the E_2' and E_4' centers, we note they have similar g values and are hydrogen-related. Such observation allowed

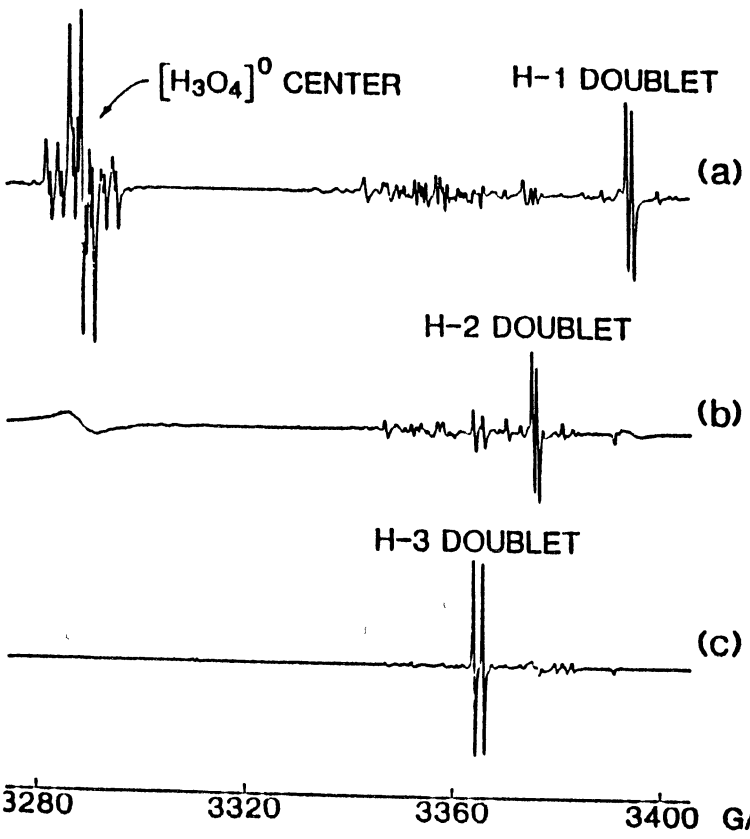

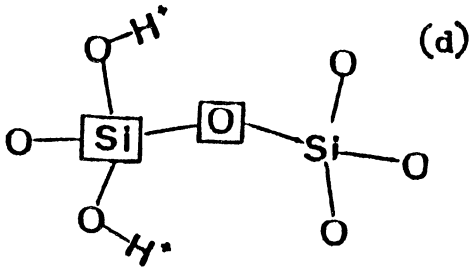

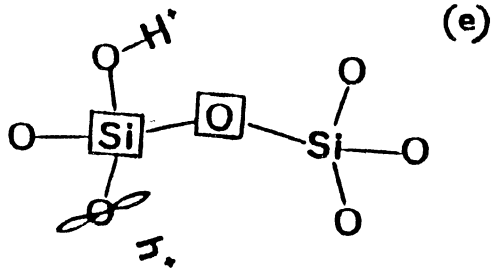

Figure 7. EPR spectra of $[H_3O_4]^0$ and H-1, H-2, and H-3 centers. Figures (a), (b), and (c) taken at 18 K, 37 K, and 57 K. Figure (d) shows the H-1 and H-2 "precursor" models. Figure (e) show the H-1 and H-2 model after a lengthy 77 K irradiation

the U-2, U-3, and U-4 centers to be assigned to the oxygen-vacancy family of defects. Support for the suggestion that these centers are hydrogen-related comes from the observation in which an H^{o} center (atomic hydrogen) decays into an U-2 and U-3 center at a given temperature. This observation suggests a mobile hydrogen can be trapped at already existing defects thus converting them to the U-2 or U-3 center.

Chen [28] modeled the U-2 and U-3 centers from observations that included the saturation of such defects beyond 100 Mrads of radiation, the negative g shifts, the presence of a single proton as seen by electron-nuclear double resonance (ENDOR) and EPR spin-flip transitions, the long spin-lattice relaxation times, the decay of the hydrogen atom center into the proposed center, and the fact that the unpaired electron in each defect is localized primarily on one silicon ion. The localization suggests two possible models, one of which could be an oxygen vacancy similar to the E type centers and the other could contain no vacancy at all.

The EPR spectra and the proposed model for the U-2 and U-3 centers can be seen in figure 8. The model is basically a variant of the $[SiO_4/Li^{+}]^{o}$ center discovered by Jani et al. [30]. The difference being that instead of a lithium compensator there is an interstitial proton in the form of an OH^{-} molecule providing the charge compensation for an extra electron trapped on a silicon ion. The difference in

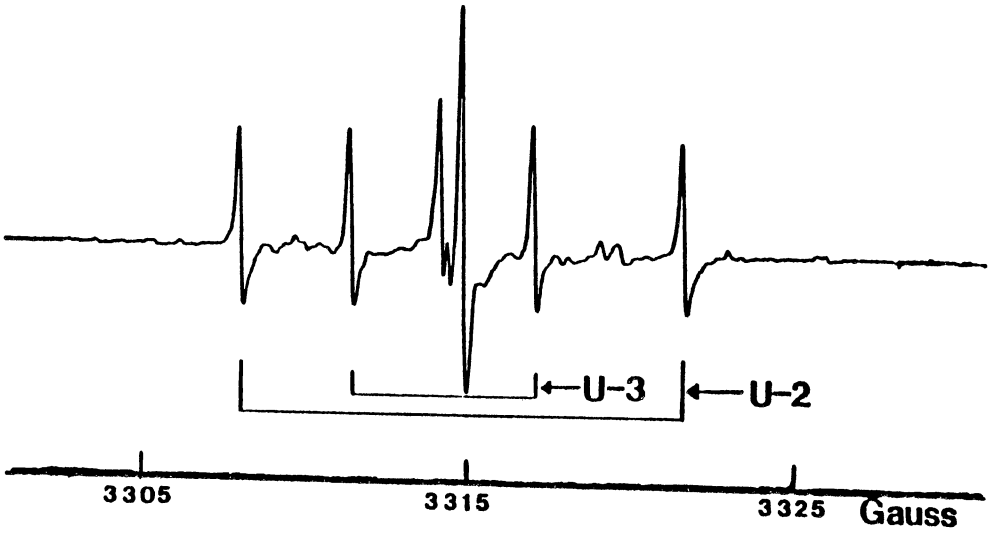

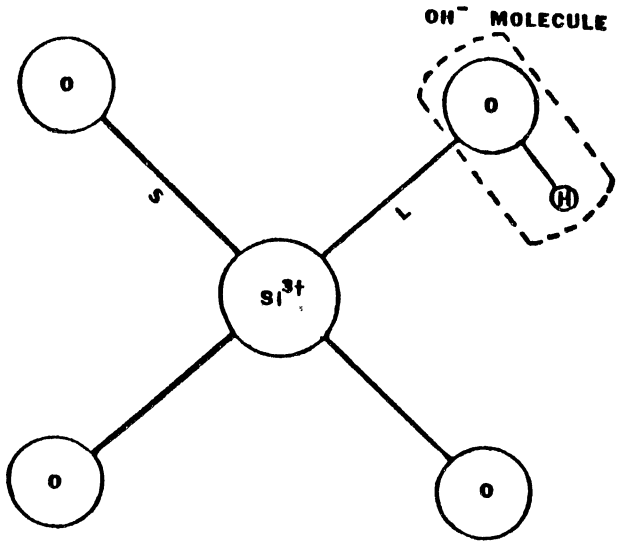

Figure 8. EPR spectra and proposed model of the U-2 and U-3 center. Data taken at 77 K with magnetic field parallel to c-axis and microwave frequency of 9.2819 GHz

the models for the U-2 and U-3 centers would be in the location of the OH^- molecule; in one case it is on the long bond side of the Si^{3+} and in the other case it is on the short bond side. Further studies of the EPR angular dependence and the ^{29}Si hyperfine interactions will completely prove or disprove these models for the U-2 and U-3 centers.

Present Study

In this study, after the introductory chapters, three topics will be covered. The first is a correlation of the EPR signal and the UV optical absorption signal of the E'' centers. This includes defect production and thermal anneal data.

The second topic is a continuation of the work by Chen [28] on the U-3 center with the goal of better identifying its model. This portion of the thesis includes angular measurements and spin-Hamiltonian parameter calculations.

The last topic includes a report on new defects produced during long irradiations at 77 K. This includes an "in-phase" and "out-of-phase" defect production study and a thermal anneal.

CHAPTER II

OPERATIONAL THEORY

Electron Paramagnetic Resonance

EPR signals arise from magnetic dipole transitions induced by an electromagnetic field. Two different approaches have been taken to explain this magnetic resonance phenomena. One such approach describes EPR spectroscopy via quantum mechanics by beginning with the Dirac four-vector description of the electronic wavefunction. This permits the concept of electron spin to evolve from relativistic and non-relativistic equations of electron motion [31].

The other approach to describing EPR spectroscopy is classical. Because the motion of a charged particle creates a magnetic field, the motion of an unpaired electron will give rise to a magnetic moment. The total magnetic moment can be derived from the motion of the electron about the nucleus of an atom (called the orbital magnetic moment) and from the "spinning of the electron about its own axis" (called the spin magnetic moment). In most cases, the total electron magnetic dipole is determined primarily by the spin magnetic moment with only a small orbital magnetic moment

contribution. From this, one can relate the magnetic moment of a free electron to the spin magnetic moment by

$$\vec{\mu} = \gamma \vec{p} = \gamma \hbar \vec{S} = g\beta \vec{S}$$

where $\vec{p}$ is the angular momentum of the electron, γ is the magnetogyric ratio = (e/(2mc)), e is the charge on the electron, m is the mass of the electron, and c is the speed of light. $\hbar$ is Plank's constant divided by 2π, $\vec{S}$ is the electron spin which can assume the quantum numbers of $\pm 1/2$, β is the Bohr magneton = $e\hbar/(2mc)$, and g is the electronic g value = 2.002319278 for a free electron.

The magnetic moment of the electron interacts with a magnetic field. The interaction energy is given by

$$-\vec{\mu} \cdot \vec{H}$$

and this gives rise to the energy level diagram shown in figure 9. The difference in energy between the two electron spin states can be matched to the available energy in a quantum of electromagnetic radiation by the following equation.

$$\Delta E = h\nu$$

Transitions may be induced between the energy levels by exposing the sample containing unpaired electrons to an electromagnetic field of frequency

$$\nu = \frac{\Delta E}{h} = \frac{g\beta H}{h}$$

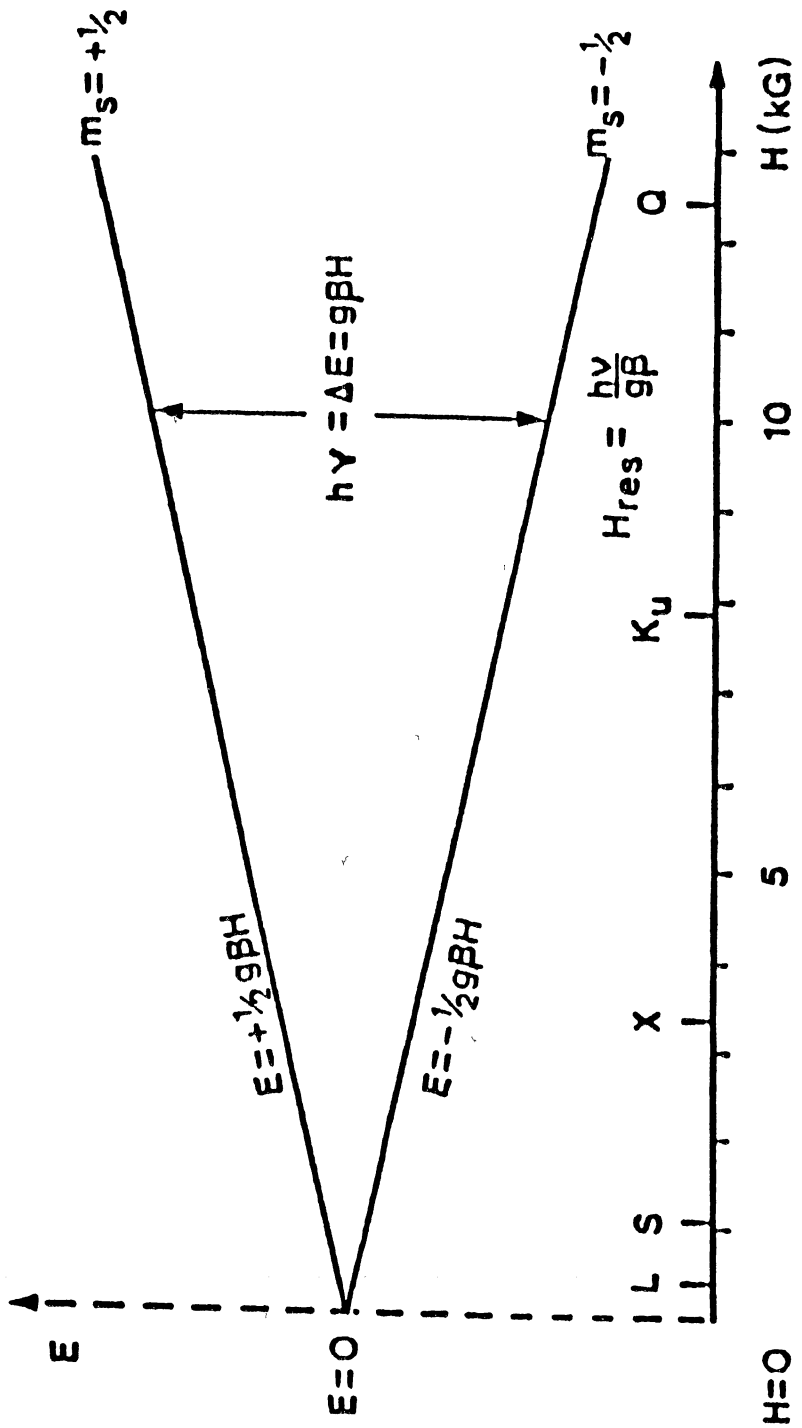

Figure 9. Energy level diagram

These transitions result in a net absorption of electromagnetic energy due to the fact that in thermal equilibrium the number of spins in the lower state is larger (by a factor of exp ($g\beta H/kT$)) than the number of spins in the upper state. One would expect the microwaves to equalize the populations of the two states. However, the spins can exchange energy with the vibrational, rotational, and translational modes of surrounding lattice ions and this tends to restore populations to the values determined by the Boltzmann factor. Thus, the resonance phenomenon can be looked on as competition between microwave-induced transitions tending to equalize the populations of the spin levels and lattice-induced transitions tending to restore a Boltzmann distribution between the levels [31].

Optical Absorption

Optical absorption signals arise when an electromagnetic field induces electric-dipole transitions and is manifested experimentally as an optical density measurement. Optical density is defined to be

$$OD = \log (I_o / I)$$

where I_o is the intensity of light incident on the sample and I is the intensity of light emerging from the sample. The intensity of light transmitted by the crystal is related

to the absorption coefficient, α , by the equation

$$I / I_o = e^{-\alpha d}$$

where d is the thickness of the crystal. Substituting the intensity ratio into the definition of optical density gives

$$OD = \log (e^{\alpha d}) = \alpha d / \ln (10)$$

This shows that the optical density is proportional to the absorption coefficient.

CHAPTER III

EXPERIMENTAL APPARATUS AND PROCEDURE

EPR Spectrometer

A ESP 300 Bruker spectrometer was used for the E'' measurements because of its software package which allowed for the reproducible measurement of signal intensities. A ER 200-SRC IBM (Bruker) spectrometer was used for the U-3 investigations because of the large spacing between pole caps which permitted a more complete angular dependence study. Both spectrometers are X-band homodyne and are equipped for ENDOR. These spectrometers consist of a magnet, magnet power supply, microwave bridge, and a separate console that contains a time base unit , signal channel, field controller, and a chart recorder as seen in figure 10. Both are equipped with computers, but the ESP 300 has a color monitor with updated software. A TE_{102} rectangular cavity was used for both studies. It has 50-G rapid scan coils and has a 50% transmittance irradiation grid and can be fitted with liquid nitrogen or liquid helium cryostats/dewars [31].

Figure 11 is a block diagram of the microwave bridge. The microwaves are produced by a klystron (1). The micro-

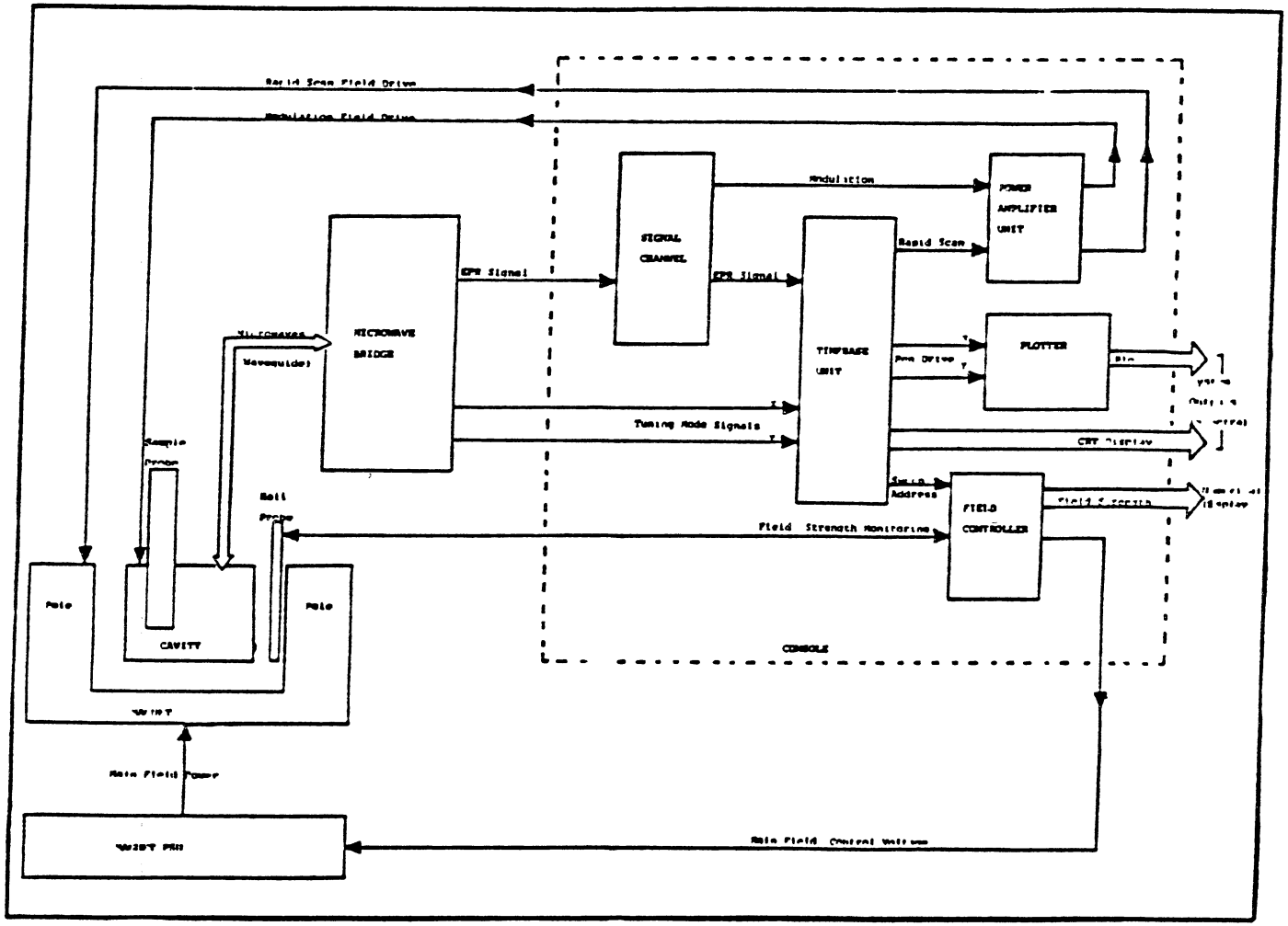

Figure 10. Block diagram for EPR spectrometer

waves are split into a power arm (2), used to both transmit the microwaves to the sample and detect the signal response, and a reference arm. In the power arm, the microwave power level is adjusted by a rotary-vane attenuator (5) and the microwaves are directed to the sample by a unidirectional microwave circulator (6). The circulator directs power from the source to the sample cavity (7) and power reflected from the cavity to the detector (8) [31].

The reference arm serves the dual purpose of biasing the detector diode and allowing phase discrimination between the absorption and dispersion components of the EPR response. The biasing power is determined by the reference arm attenuator (3) while absorption/dispersion selection is determined by the reference arm phase shifter (4) [31].

Frequency stability is acheived by locking the klystron frequency to that of the sample cavity through a feedback loop. The klystron is frequency modulated (9) by imposing a small AC signal on the klystron reflector voltage. If the klystron frequency is matched exactly to the cavity's resonant frequency, maximum power is transferred to the cavity. If the klystron's frequency drifts from the cavity's frequency, a DC correction voltage is generated by a phase-sensitive detector (10). This error voltage is applied to the klystron reflector tuning voltage and "pulls" the klystron back to the cavity frequency. Automatic frequency control (AFC) is another way to refer to this frequency stabilization feedback control loop [31].

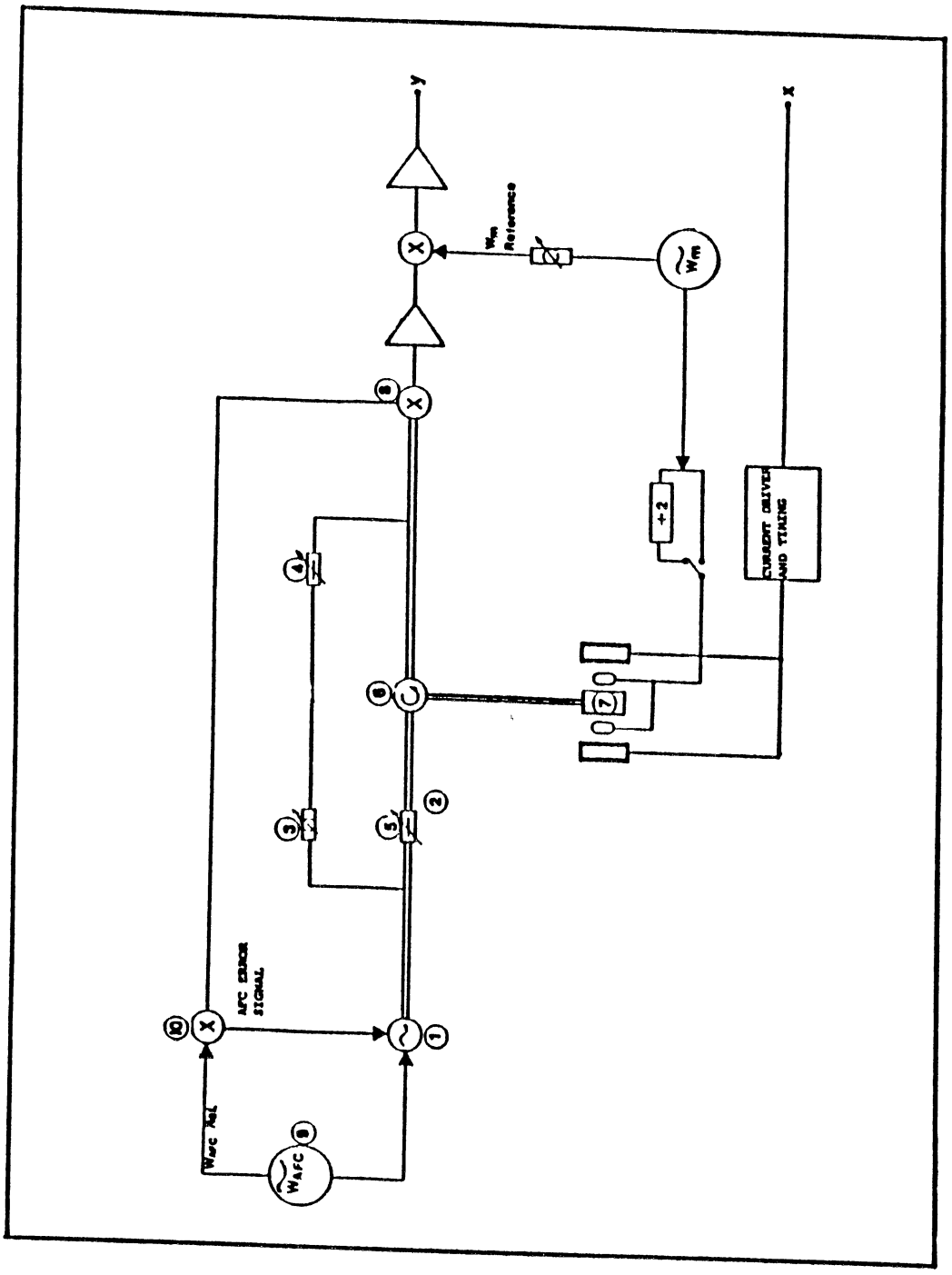

Figure 11. Block diagram for microwave bridge

During the U-3 angular dependence study, a Varian E-500 NMR Gaussmeter was used to precisely measure the magnetic field. This unit has a proton probe which is placed next to the pole cap of the magnet. It then measures the NMR resonant frequency of the internal probe sample. The proportionality of this resonant frequency to the magnetic field provides a precise reading of the magnetic field strength to seven-place accuracy. Also, a Hewlett Packard Model 5340-A frequency counter was connected directly to the microwave bridge to give seven-digit frequency values.

Optical Absorption Spectrometer

A Perkin-Elmer Model 330 spectrophotometer was used for the E'' optical-EPR correlation study. The optical layout is shown in figure 12. Light from either a deuterium lamp or a tungsten lamp is passed through a series of filters, slit mechanisms, and two grating monochromators in order to acheive a monochromatic beam of light. Once monochromatic, the beam is split by a "seesaw" device. This allows two beams into the sample compartment, one is used as a reference beam and the other is used as a sample beam. After passing through the sample compartment, the monochromatic beams are compared and their difference is converted into an electric signal by a detector such as a photomultiplier or PbS cell. The analog signal provided by the detector is then amplified and converted into a digital signal. At all subsequent stages, the signal is processed by a CPU. The

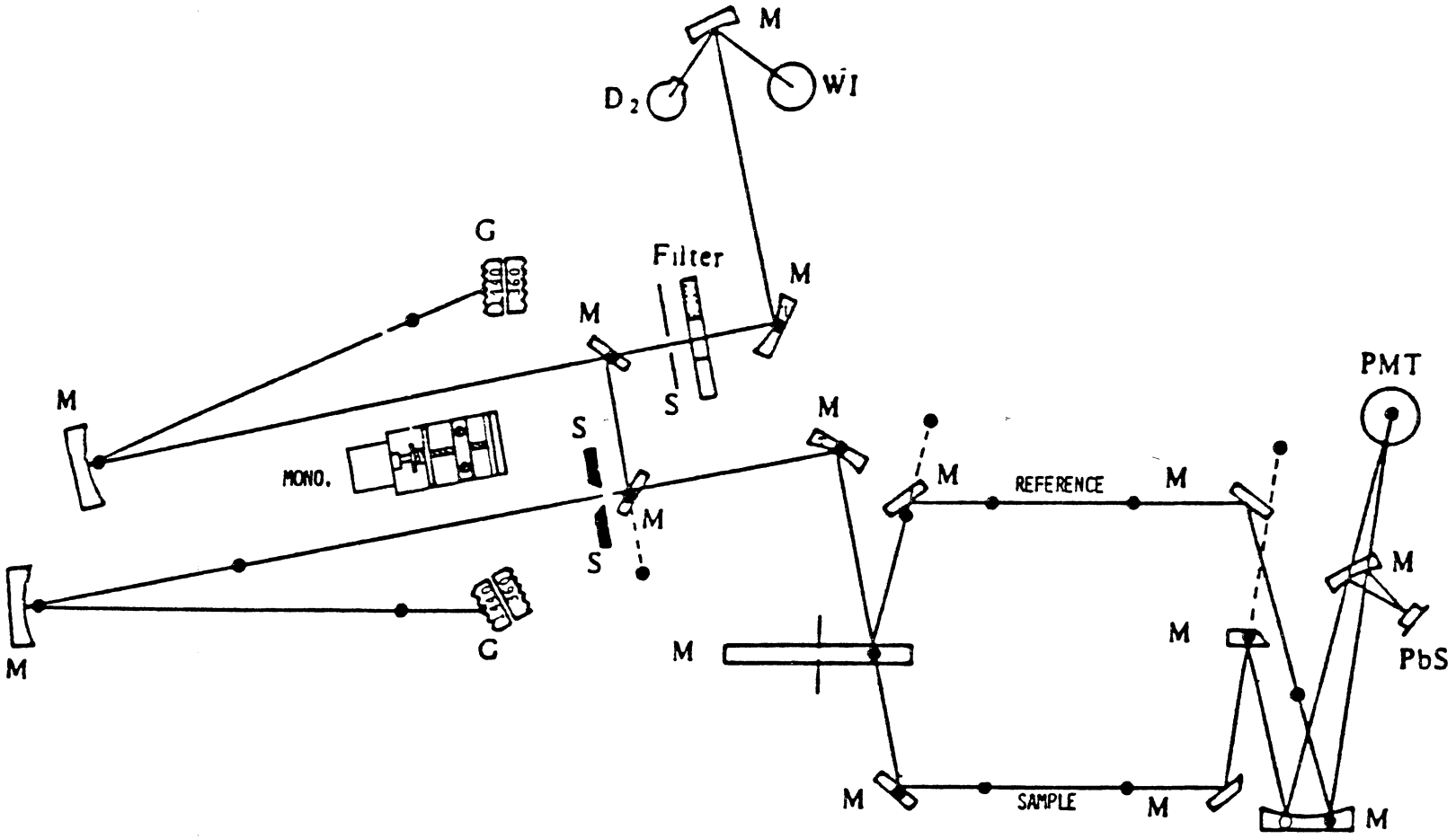

Figure 12. Optical layout for PE-330 spectrophotometer

CPU in this case is an IBM personal computer. The programs for data accumulation, graphing, and plotting were written in HT-Basic by Professor J. J. Martin.

Sample Preparation and Defect Production for the E'' Centers

The quartz crystal used for this experiment came from ThermoDynamics (Shawnee Mission, Kansas). The sample is unswept and was cut (using a diamond saw) to an optical plate of dimensions 18 x 8 x 3 mm^3 along the X,Y, and Z axes. It was then polished, on the two ends perpendicular to the Z axis, to optical quality in the Crystal Growth Laboratory at Oklahoma State University.

The defect production consisted of irradiating the sample at room temperature for long periods of time and periodically at 77 K for short periods of time. A Van de Graaff electron accelerator was the source of high-energy electrons. During the room temperature irradiations, the sample was placed on a copper block, shown in figure 13, and cooled by recirculating ice water. This block was placed 1.5 inches from the exit window of the accelerator and then irradiated with 1.75-MeV electrons at 10 μA. During the 77-K irradiations, the sample was placed along the inside wall of a styrofoam cup filled with liquid nitrogen. The cup was then placed in front of the exit window of the accelerator (always at the same distance) and irradiated (always at the same energy and current). The room temperature irradiations

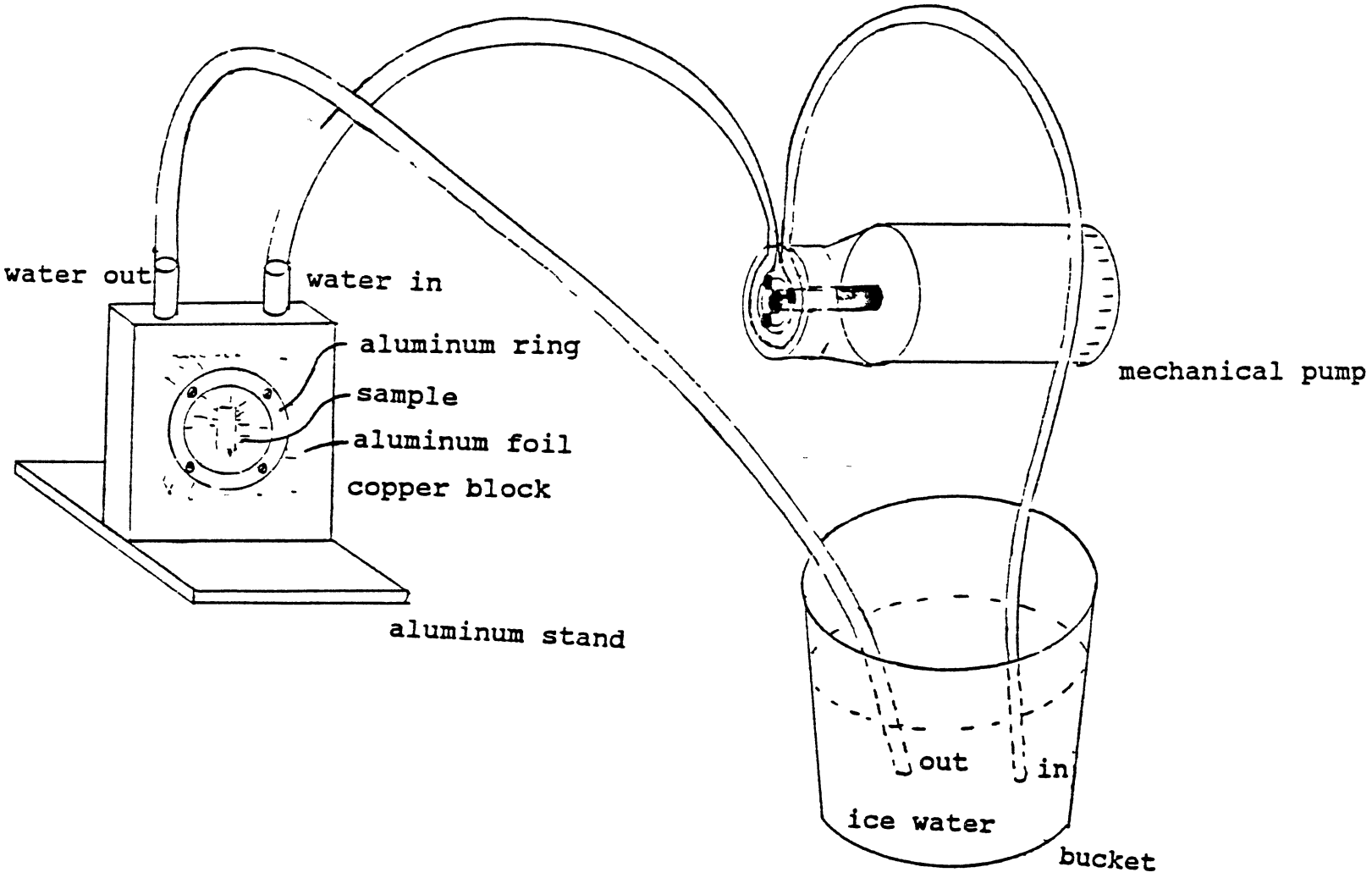

Figure 13. Cooling mechanism for room temperature irradiations

were done in 15-minute intervals for the first hour and in 2-hour intervals after that. Following each room-temperature irradiation, a 77-K irradiation was performed for 5 minutes. At all times between irradiation and subsequent monitoring of the sample, the sample was kept at 77 K. The optical absorption and EPR signals from the E'' centers were periodically monitored during a repeating sequence of irradiations. These data were always taken at room temperature.

Sample Preparation and Defect Production for the U-3 Centers and New Centers

The quartz sample used for both of these experiments came from Sawyer Research Products (Eastlake, Ohio). The samples are z growth, unswept, and were cut to an EPR size having dimensions of 8 x 2.5 x 3 mm^3 along the X, Y, and Z axes in the Crystal Growth Laboratory of Oklahoma State University.

The production of U-3 centers consisted of irradiating the sample at 77 K with a Van de Graaff electron accelerator. Specifically, a sample was placed inside and along the wall of a stryofoam cup with aluminum foil placed around it for support. The cup was then filled with liquid nitrogen and placed one inch from the exit window of the accelerator. It was then irradiated with 1.75-MeV electrons at 10 μA for up to 30 minutes. The sample was kept at 77 K throughout the course of the entire experiment.

The defect production of the new centers is the same as that used for the U-3 centers, except the new centers were irradiated for up to 4 hours and not 30 minutes as stated for the U-3 centers. During the irradiation process, the styrofoam cups were changed out at 6-minute intervals because the ozone build-up in the styrofoam cup could ignite and cause a massive explosion. Again, the sample was kept at 77 K throughout the course of the experiment.

Thermal Anneal Procedure for the E'' Centers

In this experiment a tubular Hoskins electric furnace equipped with an Omega Model 6000 temperature controller was used. A chromel-alumel thermocouple placed in the middle of the coiled heating element of the furnace provided a feed-back signal for the temperature regulation. Another chromel-alumel thermocouple was placed inside of the stain-less steel tube holding the sample.

In detail, the controller was set to a desired temper-ature. After thermal equilibrium was achieved (in roughly 5 minutes), the sample was pushed into the middle of the furn-ace. At that instant, a timer was set for 25 minutes in order to get an average 15 minute pulsed anneal. It took approximately 10 minutes for the sample to reach the set temperature. After the 25 minutes had elapsed the stainless steel tube containing the sample was pulled out of the furnace slowly to prevent thermal shock. The sample was removed after the tube reached room temperature. The sample

was then placed in liquid nitrogen for storage. Just prior to taking optical absorption and EPR data, the sample was returned to room temperature.

Thermal Anneal Procedure for the U-3 Centers and New Centers

For this experiment a variable temperature pulsed anneal was done outside the EPR cavity. This was accomplished by using the nitrogen gas flow system in figure 14. Nitrogen gas flows from the tank through a regulation valve into a double heat exchanger filled with liquid nitrogen. Once the gas passes the heat exchanger it then flows into a transfer tube containing an electric heater. At the end of the transfer tube lies a cryostat equipped with a copper-constantan thermocouple. The thermocouple and heater are connected to a Bruker ER-4111VT variable temperature unit. This unit, when the temperature and heating current is set, will regulate at the chosen temperature.

In detail, the procedure begins by placing the EPR-size sample in a Delrin-tipped hollow stainless steel rod (used in finger Dewars during 77-K EPR measurements) while submerged in liquid nitrogen. The cryostat temperature is brought down to 77 K and the rod, with sample, is quickly removed from the liquid nitrogen and placed inside of the cryostat less than a millimeter from the thermocouple. Then the temperature, gas flow, and heater current are set and regulated accordingly. After 5 minutes have elapsed at that

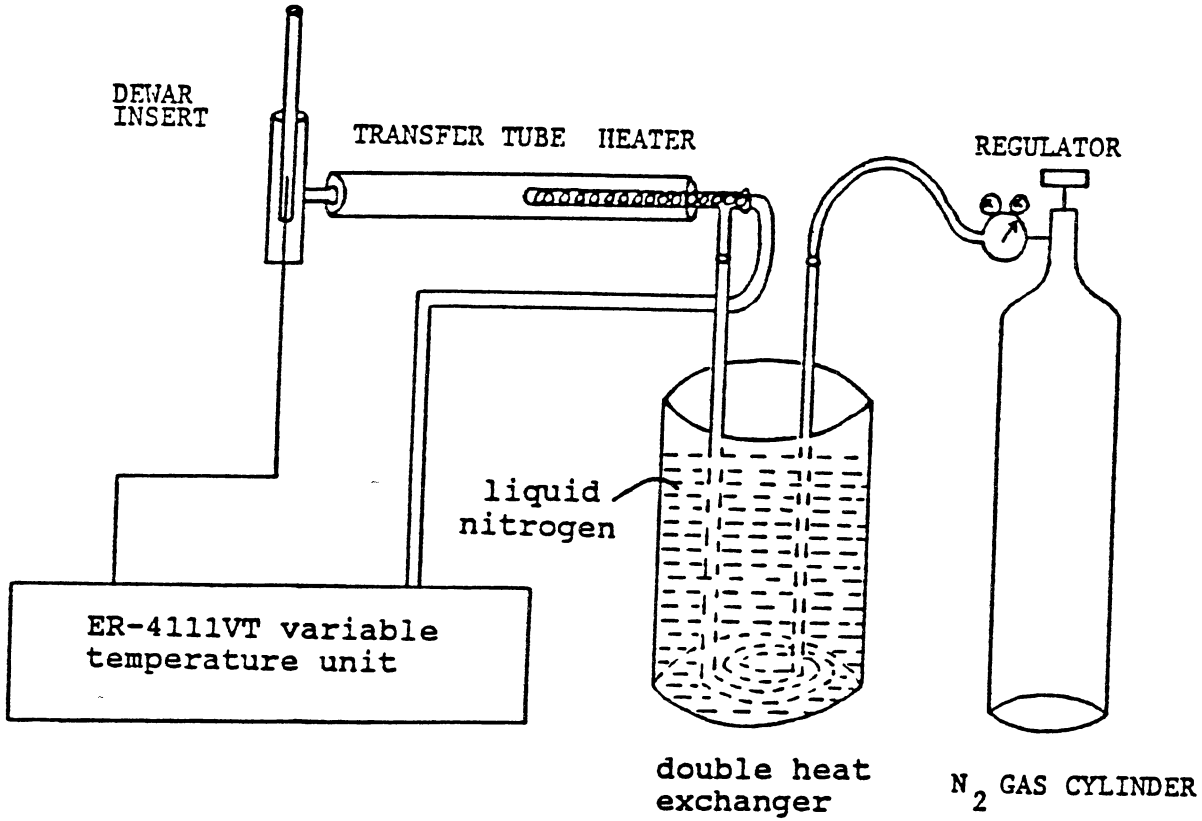

Figure 14. Nitrogen gas flow system

given temperature, the temperature of the cryostat is brought back down to 77 K and the rod ,with sample, is removed quickly and placed in liquid nitrogen. The intensities of the EPR signals are then monitored.

CHAPTER IV

THEORETICAL ANALYSIS USED FOR THE U-3 CENTERS

The spin system that describes the U-3 centers has an electronic spin of S = 1/2 and a nuclear spin of I = 1/2. The following spin Hamiltonian describes this system.

$$\mathcal{H} = \beta \bar{S} \cdot \overleftrightarrow{g} \cdot \bar{H} + h\bar{S} \cdot \overleftrightarrow{A} \cdot \bar{I} - g_N \beta_N \bar{I} \cdot \bar{H}$$

The first term represents the electron Zeeman interaction, the second term is the nuclear hyperfine interaction, and the last term is the nuclear Zeeman interaction.

To be able to numerically analyze the spin-Hamiltonian, the equation must be converted into a proper coordinate system. The coordinate systems used are:

X,Y,Z: Coordinate system for the magnetic field where H is parallel to the Z axis.

X_c, Y_c, Z_c: Coordinate system for the crystal.

X_g, Y_g, Z_g: Coordinate system for the g tensor.

X_1, Y_1, Z_1: Coordinate system for the A tensor.

These coordinate systems can now be used to rewrite the spin Hamiltonian.

$$\mathcal{H} = \beta[g_x S_{Xg} H_{Xg} + g_y S_{Yg} H_{Yg} + g_z S_{Zg} H_{Zg}] + h[A_x S_{X1} I_{X1} + A_y S_{Y1} I_{Y1} + A_z S_{Z1} I_{Z1}] - g_n \beta_n H I_Z$$

The g and A tensors must have their coordinate systems transformed to the magnetic field coordinate system by way of 3 x 3 rotation matrices [TG] and [TH] defined by:

$$\begin{bmatrix} X_g \\ Y_g \\ Z_g \end{bmatrix} = [TG] \begin{bmatrix} X \\ Y \\ Z \end{bmatrix} \quad \text{and} \quad \begin{bmatrix} X_1 \\ Y_1 \\ Z_1 \end{bmatrix} = [TH] \begin{bmatrix} X \\ Y \\ Z \end{bmatrix}$$

[TG] and [TH] contain Euler angles and involve three successive rotations performed in a specific sequence. The spin and magnetic fields are transformed in the same way.

$$\begin{bmatrix} S_{Xg} \\ S_{Yg} \\ S_{Zg} \end{bmatrix} = [TG] \begin{bmatrix} S_X \\ S_Y \\ S_Z \end{bmatrix} \quad \text{and} \quad \begin{bmatrix} H_{Xg} \\ H_{Yg} \\ H_{Zg} \end{bmatrix} = [TG] \begin{bmatrix} 0 \\ 0 \\ H \end{bmatrix}$$

The spin Hamiltonian can now be written in the magnetic field coordinate system.

$$\mathcal{H} = W1S_X + W2S_Y + W3S_Z + W4S_XI_X + W5S_XI_Y + W5S_YI_X + W6S_XI_Z + W6S_ZI_X + W7S_YI_Y + W8S_ZI_Y + W8S_YI_Z + W9S_ZI_Z - g_n\beta_n H I_Z$$

where

$$W1=\beta H[g_x TG(1,1)TG(1,3)+g_y TG(2,1)TG(2,3)+g_z TG(3,1)TG(3,3)]$$

$$W2=\beta H[g_x TG(1,2)TG(1,3)+g_y TG(2,2)TG(2,3)+g_z TG(3,2)TG(3,3)]$$

$$W3=\beta H[g_x TG(1,3)TG(1,3)+g_y TG(2,3)TG(2,3)+g_z TG(3,3)TG(3,3)]$$

$$W4=h[A_X TH(1,1)TH(1,1)+A_Y TH(2,1)TH(2,1)+A_Z TH(3,1)TH(3,1)]$$

$$W5=h[A_X TH(1,2)TH(1,1)+A_Y TH(2,2)TH(2,1)+A_Z TH(3,2)TH(3,1)]$$

$$W6=h[A_X TH(1,3)TH(1,1)+A_Y TH(2,3)TH(2,1)+A_Z TH(3,3)TH(3,1)]$$

$$W7=h[A_X TH(1,2)TH(1,2)+A_Y TH(2,2)TH(2,2)+A_Z TH(3,2)TH(3,2)]$$

$$W8=h[A_X TH(1,2)TH(1,3)+A_Y TH(2,2)TH(2,3)+A_Z TH(3,2)TH(3,3)]$$

$$W9=h[A_X TH(1,3)TH(1,3)+A_Y TH(2,3)TH(2,3)+A_Z TH(3,3)TH(3,3)]$$

Using the raising and lowering operators, given by $S_+= S_X + iS_Y$, $S_-= S_X - iS_Y$, $I_+= I_X + iI_Y$, and $I_-= I_X - iI_Y$, we can change the Hamiltonian to:

$$\mathcal{H} = W3S_Z + S_+[(W1-iW2)/2] + S_-[(W1+iW2)/2] + S_+I_+[(W4-2iW5-W7)/4] + S_+I_-[(W4+W7)/4] + S_-I_+[(W4+W7)/4] + S_-I_-[(W4+2iW5-W7)/4] + S_+I_Z[(W6-iW8)/2] + S_-I_Z[(W6+iW8)/2] + S_ZI_+[(W6-iW8)/2] + S_ZI_-[(W6+iW8)/2] + W9S_ZI_Z - g_n\beta_n HI_Z$$

The spin-Hamiltonian can be further simplified to

$$\mathcal{H} = W3S_Z + S_+Q1^* + S_-Q1 + S_+I_+Q2^* + S_+I_-Q3 + S_-I_+Q3 + S_-I_-Q2 + S_+I_ZQ4^* + S_-I_ZQ4 + S_ZI_+Q4^* + S_ZI_-Q4 + W9S_ZI_Z - g_n\beta_n HI_Z$$

where

$$Q1 = (W1 + iW2)/2$$

$$Q2 = (W4 - W7 + 2iW5)/4$$

$$Q3 = (W4 + W7)/4$$

$$Q4 = (W6 + iW8)/2.$$

Since the proton (H^+) nucleus has I = 1/2, the basis set chosen is $|M_S = \pm 1/2, M_I = \pm 1/2\rangle$. This basis set consists of 4 vectors which allows one to write the

Hamiltonian in a 4x4 matrix form. Then the eigenvalue energy levels are obtained by diagonalizing this matrix. Since the Hamiltonian is hermitian, only the lower half of the matrix is needed to find the eigenvalues.

The notation for the lower half of the Hamiltonian matrix is given in table 1. The non-zero elements of the matrix are given below:

$A(1,1) = W3/2 + W9/4 + g_n\beta_n H/2$

$A(2,1) = Q4/2$

$A(3,1) = Q1 + Q4/2$

$A(4,1) = Q2$

$A(2,2) = W3/2 - W9/4 + g_n\beta_n H/2$

$A(3,2) = Q3$

$A(4,2) = Q1 - Q4/2$

$A(3,3) = -W3/2 - W9/4 - g_n\beta_n H/2$

$A(4,3) = -Q4/2$

$A(4,4) = -W3/2 + W9/4 + g_n\beta_n H/2$

TABLE I

LOWER HALF OF THE SPIN HAMILTONIAN MATRIX

	|1/2,1/2>	|1/2,-1/2>	|-1/2,1/2>	|-1/2,-1/2>
|1/2,1/2>	A(1,1)			
|1/2,-1/2>	A(2,1)	A(2,2)		
|-1/2,1/2>	A(3,1)	A(3,2)	A(3,3)	
|-1/2,-1/2>	A(4,1)	A(4,2)	A(4,3)	A(4,4)

CHAPTER V

EXPERIMENTAL METHOD AND RESULTS FOR THE EPR E''CENTER AND THE 218 nm OPTICAL ABSORPTION SIGNAL CORRELATION

Defect Production Correlation

Prior to beginning the E'' correlation study, an optical plate had to be selected that could be used in both the EPR and optical absorption spectrometers. The plate had to be small enough to fit inside the EPR cavity and had to be large enough to give a good optical signal. Once the plate was selected, it was annealed at 500^{o}C for an hour, as a precaution, to remove all pre-existing defects.

Next, the plate was irradiated at room temperature (actually 0^{o}C) for a given time. Following this room temperature irradiation, the plate was then given a short irradiation at 77 K. A precise description of the defect production is given in Chapter 3.

After the two initial irradiations, an optical absorption spectrum was obtained. The plate was then transfered to the EPR spectrometer for observation. All of the spectra were taken at room temperature and, between all steps, the sample was kept cold at 77 K to maintain the

defect intensity. Also, between all steps, the plate was wrapped in aluminum foil to prevent optical bleaching.

The optical absorption and EPR spectra were taken at 15-minute irradiation intervals for the first hour, 30-minute irradiation intervals for the second hour, 60-minute irradiation intervals for two hours, and 2-hour irradiation intervals for the last twenty hours. An optical absorption spectrum representing the total accumulated defect concentration after each irradiation step can be seen in figure 15.

This figure shows an optical absorption band, taken with the light beam propagating along the c axis, centered approximately on 218 nm. It, along with a shoulder at 201 nm, grows with increased doses of radiation. The most intense trace, containing a pronounced peak at 218 nm, corresponds to 24 hours of irradiation. Figure 16 gives the photon energy, for selected irradiation intervals, for these two bands at 5.7 eV and 6.2 eV, respectively. In the next paragraph, the 218-nm band is shown to correlate with the E'' center EPR signal.

Figure 17 represents the EPR spectra obtained from E'' centers after 15 minutes and after 24 hours of irradiation. These data were taken with the c axis parallel to the magnetic field. The E_1'' center is the inner doublet split by 5.01 G and is more intense than the E_2'' center which is the middle doublet split by 11.02 G and the E_3''center which is the outer doublet split by 17.88 G. A detailed de-

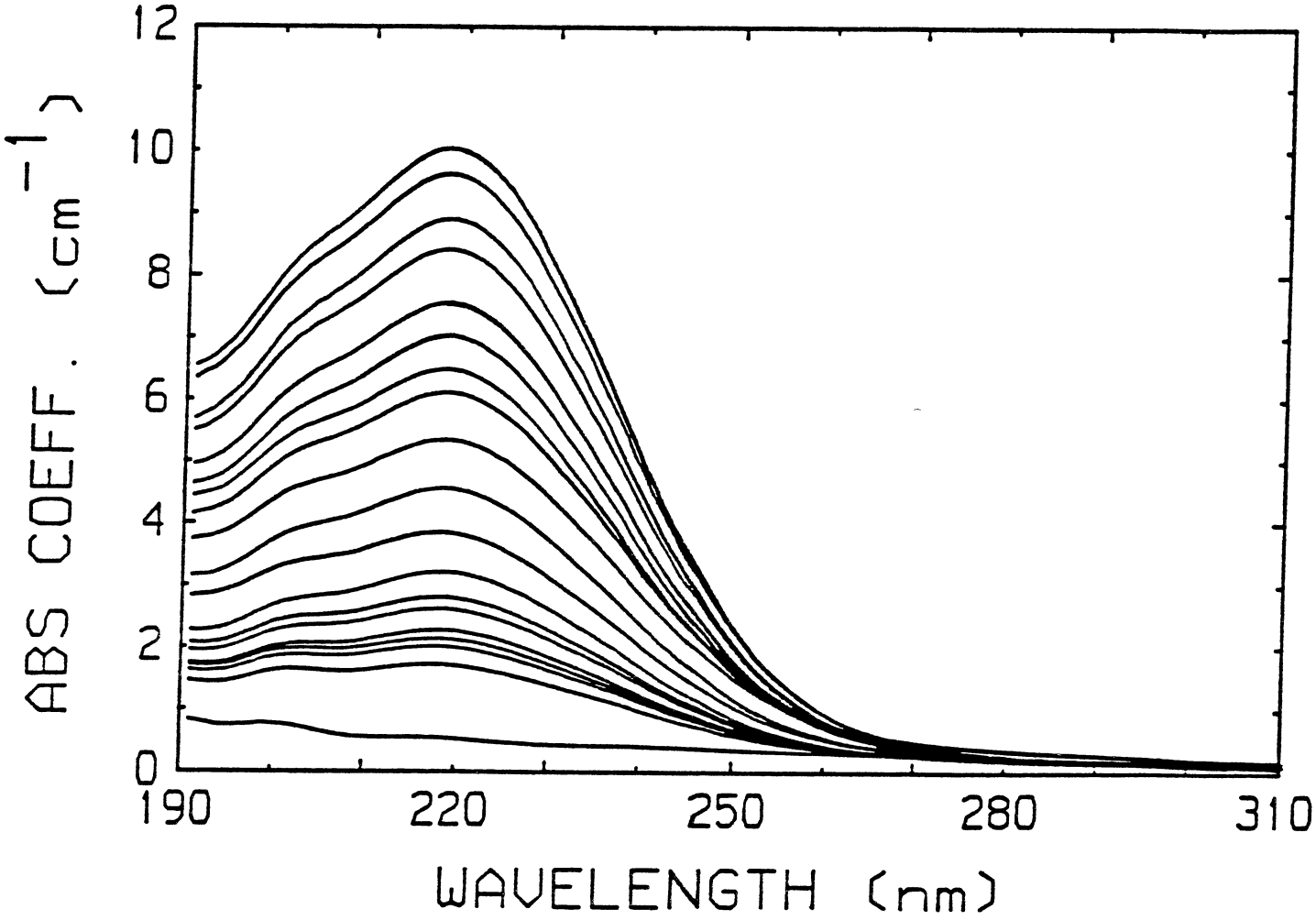

Figure 15. Optical absorption spectra of defect concentrations after each irradiation step. Top spectrum represents 24 hour irradiation

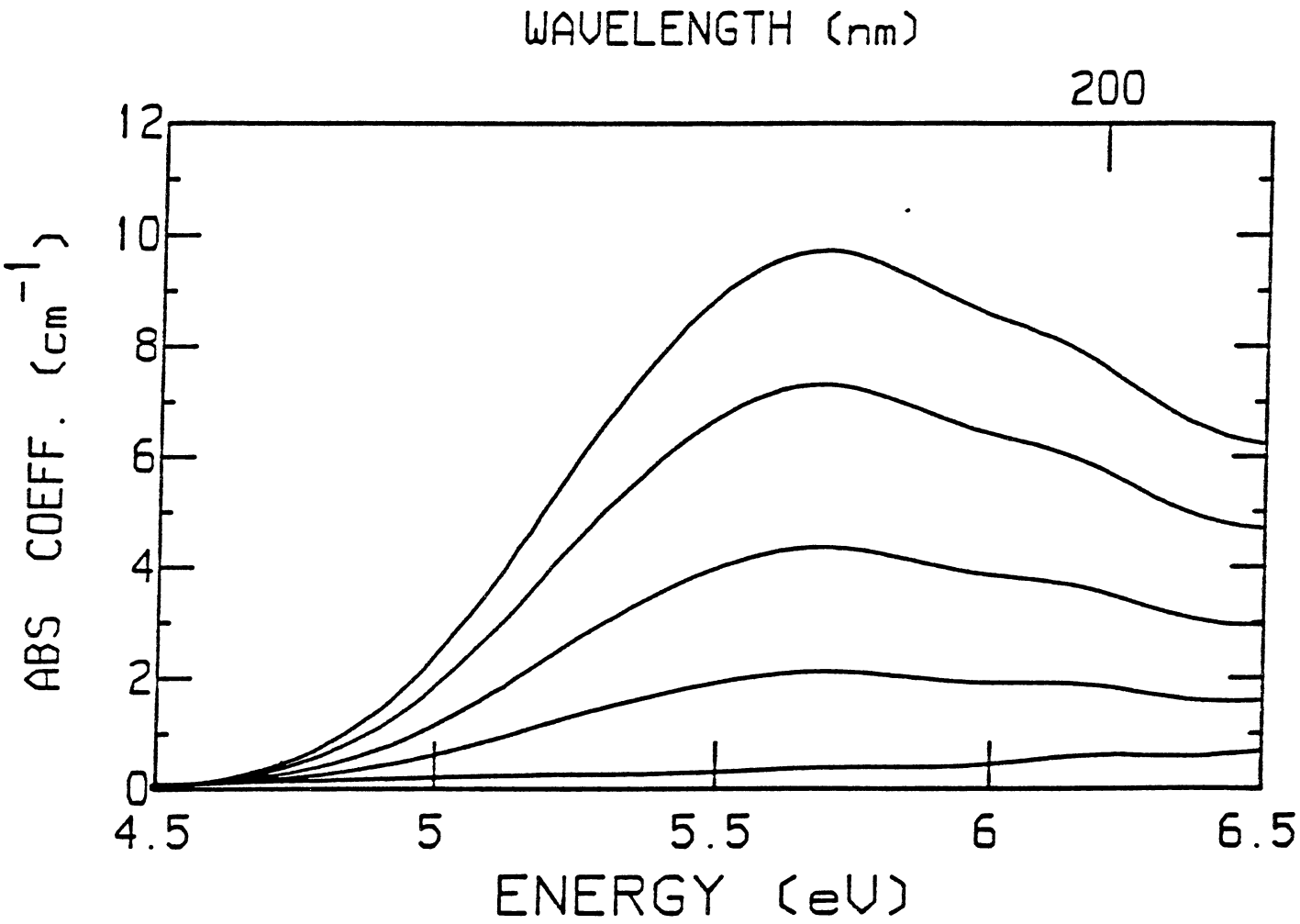

Figure 16. Optical absorption spectra providing photon energy for selected irradiation times. Top spectrum represents 24 hour irradiation

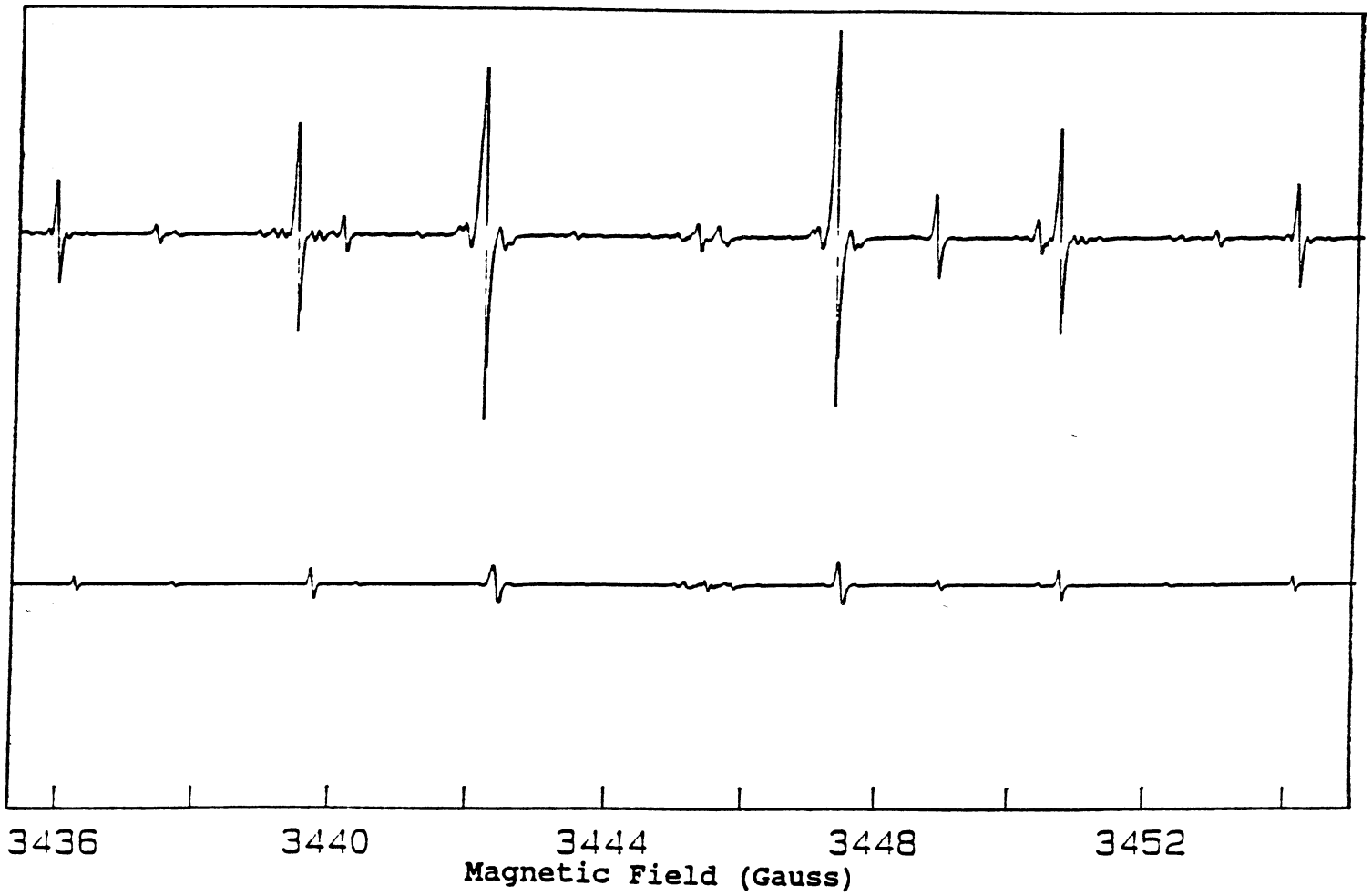

Figure 17. EPR E'' spectra representing 15 minute irradiation (bottom) and 24 hour irradiation (top)

scription of the E'' center spectra and their proposed models are given in Chapter 1.

After each step in the irradiation sequence, the intensity (i.e., concentration) of each E'' center was obtained. These results were, in turn, compared to the intensity (i.e., concentration) of the 218-nm optical absorption band.

The intensity of an EPR center was obtained as follows. Each line (first derivative) in the spectrum was integrated to recreate the original absorption spectrum. In the case of the E'' centers, there were two lines in each c-axis spectrum. Then, the individual peak heights were directly measured to arrive at a cumulative signal intensity representing the defect's concentration. Following the integration step, a baseline correction was performed. This involved doing a cubic fit on the baseline of the integrated spectrum, and then subtracting the cubic-fit baseline to get a straight baseline. The EPR spectra manipulations were accomplished using software provided by Bruker.

The intensity of the optical absorption spectrum was measured at 218 nm. Once all intensities for the EPR and optical spectra were provided, they were normalized to one and plotted accordingly.

Figure 18 shows the correlation of intensities of the EPR E_1'' center and the 218-nm optical absorption peak. This figure contains data up to 24 hours of irradiation. It is apparent that the first 2 hours of irradiation gives a

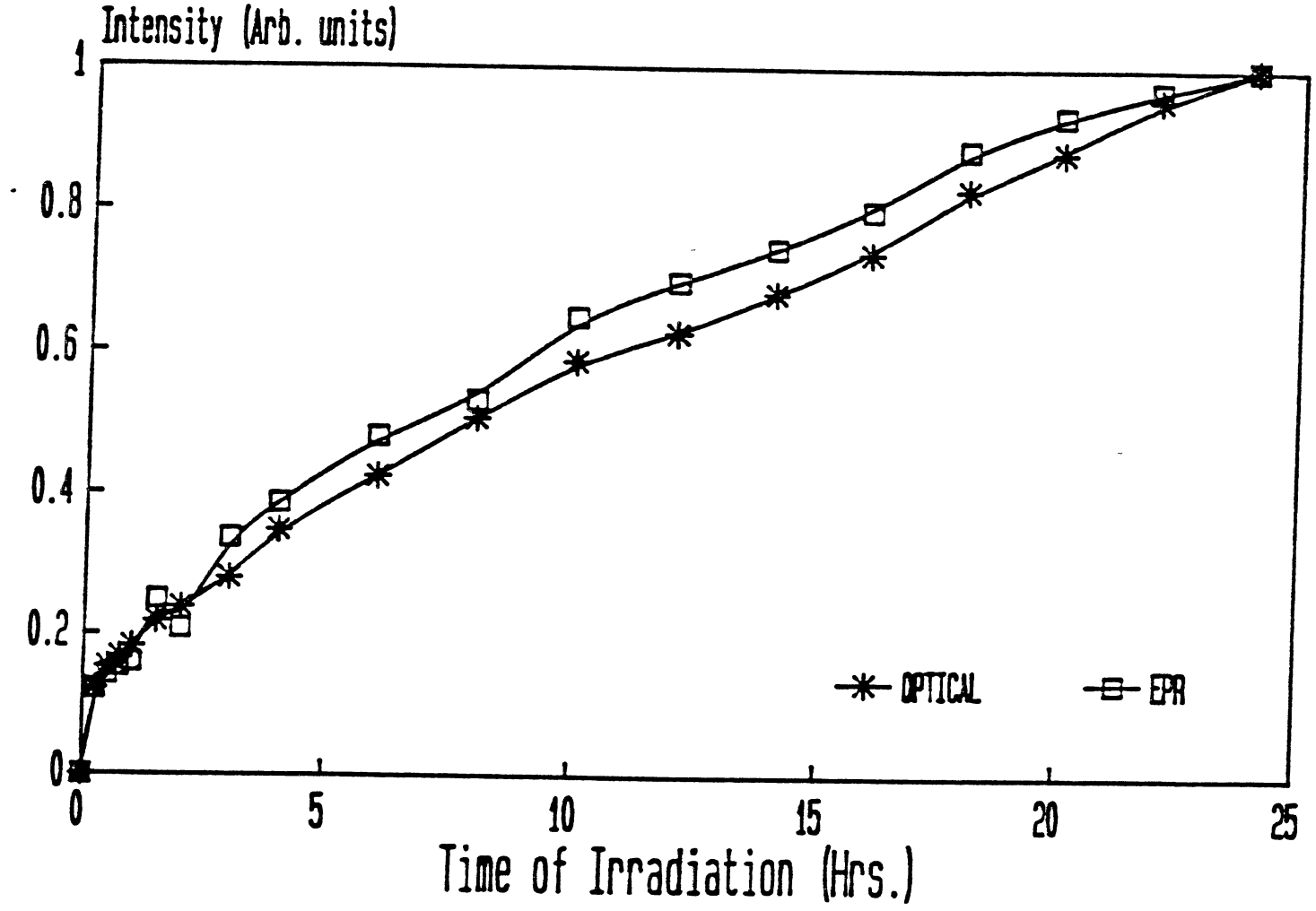

Figure 18. Defect production correlation between intensities for EPR E_1'' center and 218nm optical absorption peak

sharp defect production as opposed to the last 22 hours of irradiation that give a nearly linear defect production. This figure shows the two production curves are very similar.

Figure 19 shows the correlation of intensities between the EPR E_2'' center and the 218-nm optical absorption line. Again, one sees the same production behavior including the initial sharp growth evolving into a later linear growth. Also, figure 20 shows the correlation between the EPR E_3'' center and the 218-nm optical absorption line. Figure 21 gives the correlation between the averaged EPR E'' centers and the 218-nm optical absorption line.

Thermal Anneal Correlation

A thermal anneal was performed on the quartz plate after the 24 hours of defect production. This anneal was accomplished by holding the plate at a desired temperature for a given time and then returning to room temperature to monitor both the EPR and optical absorption spectra before proceeding on to the next higher anneal temperature.

Specifically, the sample was wrapped in aluminum foil and placed inside a furnace and heated slowly, approximately 10 minutes, to a desired temperature. The sample remained at that temperature for 15 minutes. At the end of this time, the sample was cooled to room temperature, placed in liquid nitrogen, transferred to the optical and EPR spectrometers for observation. Between all stages, the

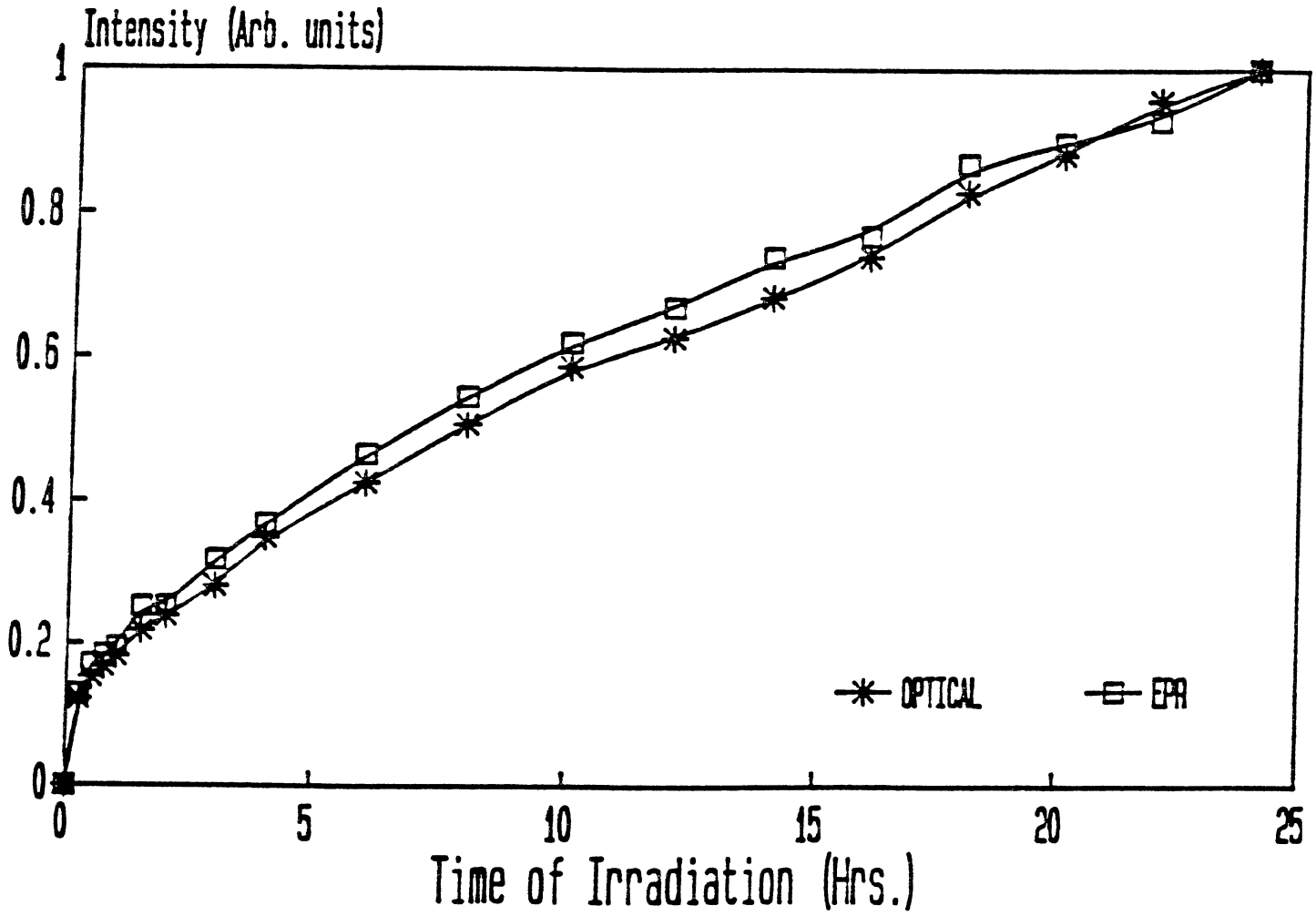

Figure 19. Defect production correlation between intensities for EPR E_2'' center and 218nm optical absorption peak

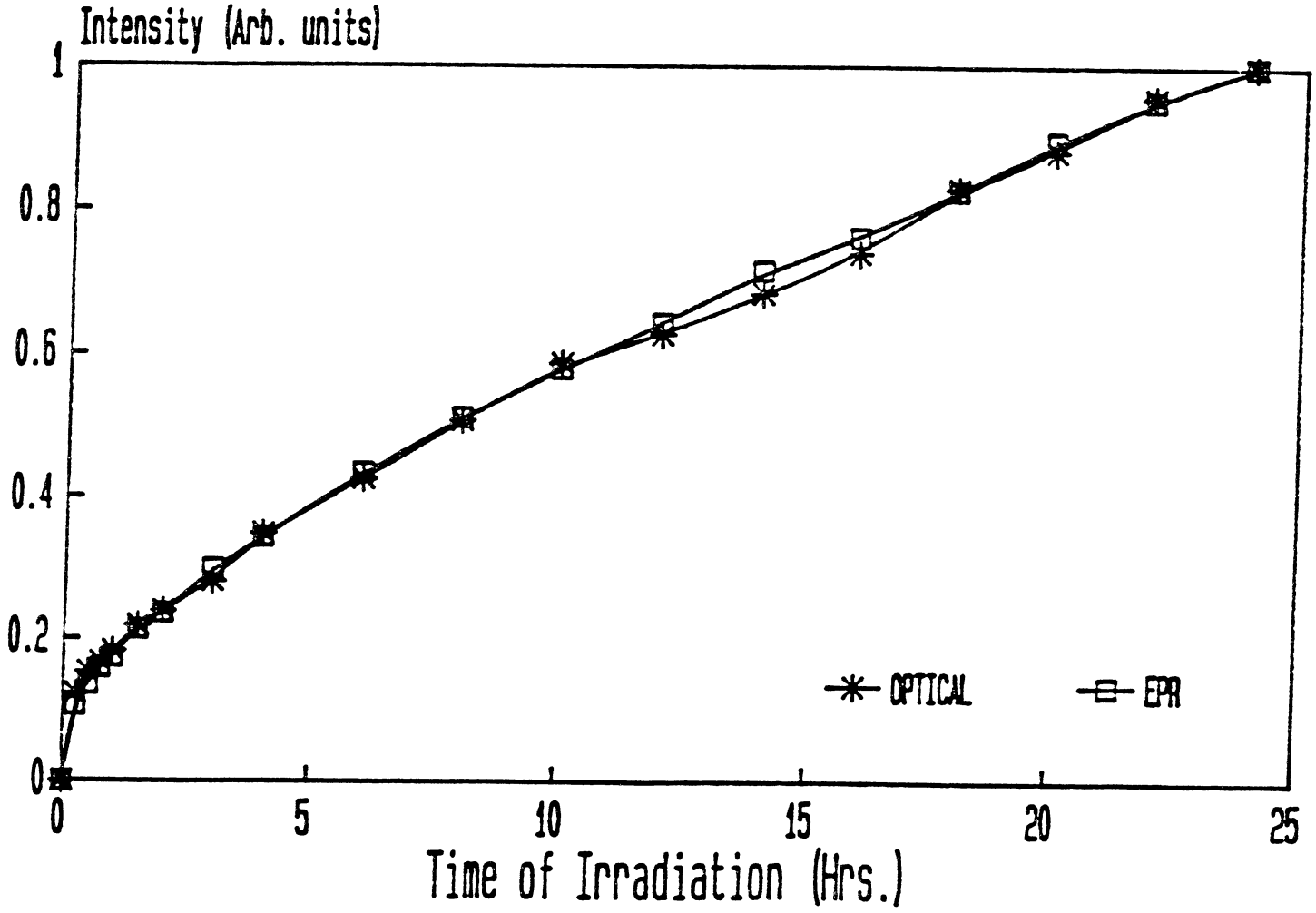

Figure 20. Defect production correlation between intensities for EPR E_3'' center and 218nm optical absorption peak

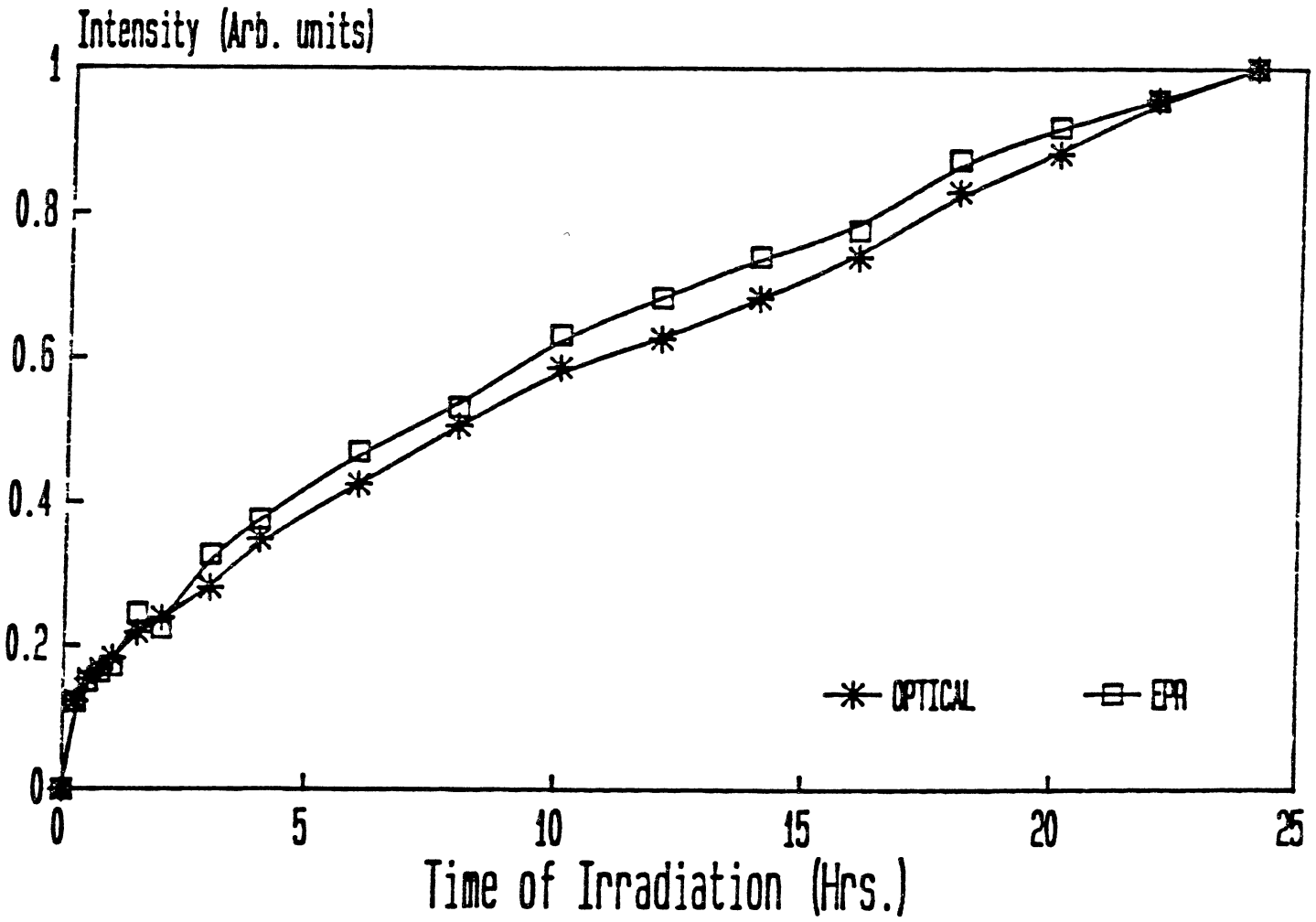

Figure 21. Defect production correlation between intensities for averaged EPR E''centers and 218nm optical absorption peak

sample was kept cold at 77 K and wrapped in aluminum foil. The spectra were taken after anneals at 20°C intervals starting at room temperature (25°C) and ending at 475°C. A detailed description of the thermal anneal set up is given in Chapter 3.

The intensities of the EPR and optical signals were measured, then normalized to one and plotted accordingly. Figure 22 represents a correlation of signal intensities between the averaged EPR E'' centers, the EPR E_1'center, and the optical absorption lines at 218 nm and 201 nm. The E_1'' center anneals out at 105°C while the E_2'' and E_3'' centers anneal out at 70°C and 110°C. At 100°C the EPR E_4' center appears. It anneals out at 200°C. Beyond 200°C, the E_1' center grows in and reaches a maximum intensity at 300°C before annealing out at 475°C. Correspondingly, the 218-nm optical absorption line anneals out at 100°C while the 201-nm optical absorption grows in at 200°C and reaches a maximum absorbance at 300°C before annealing out at 475°C.

The thermal anneal correlation shows the optical absorption bands to correlate nearly perfectly with the EPR E'' and E_1' centers. Futhermore, the thermal anneal shows no EPR or optical signals stable beyond 475°C, indicating a successful defect anneal.

Discussion

The goal of this experiment was to correlate the EPR E'' signal intensity to the 218-nm optical absorption signal

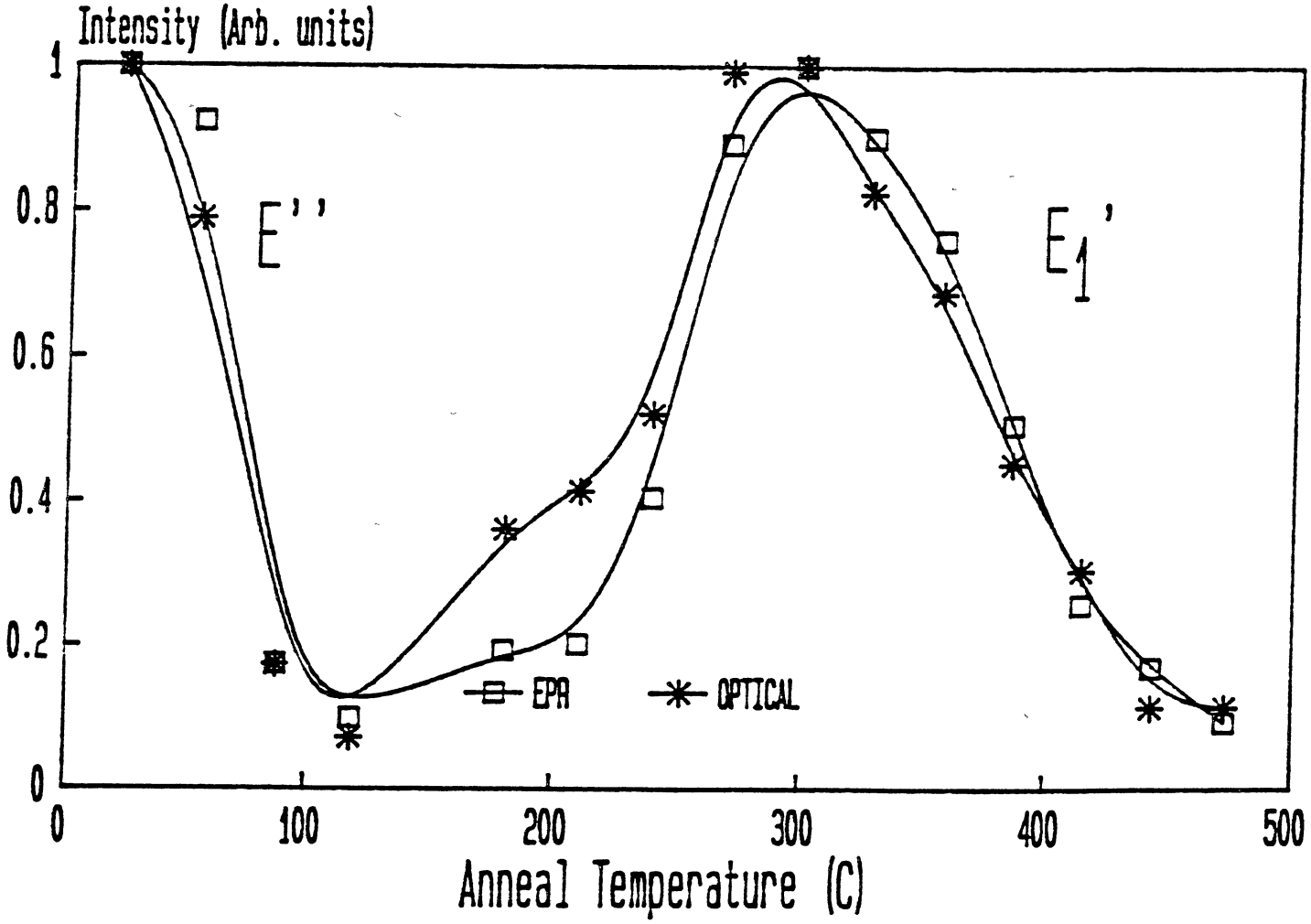

Figure 22. Thermal anneal correlation for the averaged EPR E''center, EPR E_1' center, and optical absorption peaks at 218nm and 201nm

intensity. Based on the experimental results and with prior knowledge of the EPR E'' centers, the correlation was successful. This, in turn, verifies the results suggested by Mitchell and Paige [32,33] and Arnold [34,35].

Mitchell and Paige [32,33] measured the optical absorption of neutron and X-ray irradiated quartz. They observed two bands in the UV region, at 217.5 and 163.1 nm, and labeled them the C and E bands. Their evidence led them to suggest that the C band might be due to an electron trapped in an oxygen vacancy and that the E band might be due to the related interstitial oxygen ion.

Arnold [34] irradiated quartz with 2-MeV electrons at temperatures near 77 K. This produced an optical absorption band at 220 nm (i.e., the C band). He suggested that this was a displacement process where the production rate of the defect increases with faster crystal growth rates. In a second paper, Arnold [35] concluded that the C band was due to the displacement of oxygen ions where the displacement energies correlated with the crystal growth rates.

Collective suggestions from the above mentioned references allows one to model a defect that contains trapped electrons and oxygen vacancies. The EPR E'' centers best fit this model because they are oxygen vacancies with associated unpaired electrons, thus, giving rise to the correlation. A Detailed descriptions for the E'' centers are given in Chapter 1.

CHAPTER VI

EXPERIMENTAL METHOD AND RESULTS FOR THE U-3 CENTER

Angular Dependence

Before beginning the U-3 center angular dependence study, an EPR-size quartz crystal was selected. This crystal was heated to 500°C for an hour to anneal all existing defects. Next, the crystal was irradiated for 30 minutes with 1.75-MeV electrons while being kept at 77 K. It was then annealed to 137 K (anneal condition provided by Chen [28]) to enlarge the U-3 center and, subsequently, to reduce the U-2 center. A detailed description of the defect production and thermal anneal is given in Chapter 3.

After the 137 K anneal and when the c-axis is parallel to the magnetic field, the U-3 center appears in the "out-of-phase" condition and exhibits a hyperfine splitting of 5.7 G. The U-3 center is shown in figure 23. After the sample was prepared, an angular dependence study was performed.

The angular dependence entailed aligning the magnetic field parallel to the c axis. Once aligned, the magnetic field was rotated in 5° intervals up to 70° on each side of the c-axis. The high-field line splits into three separate

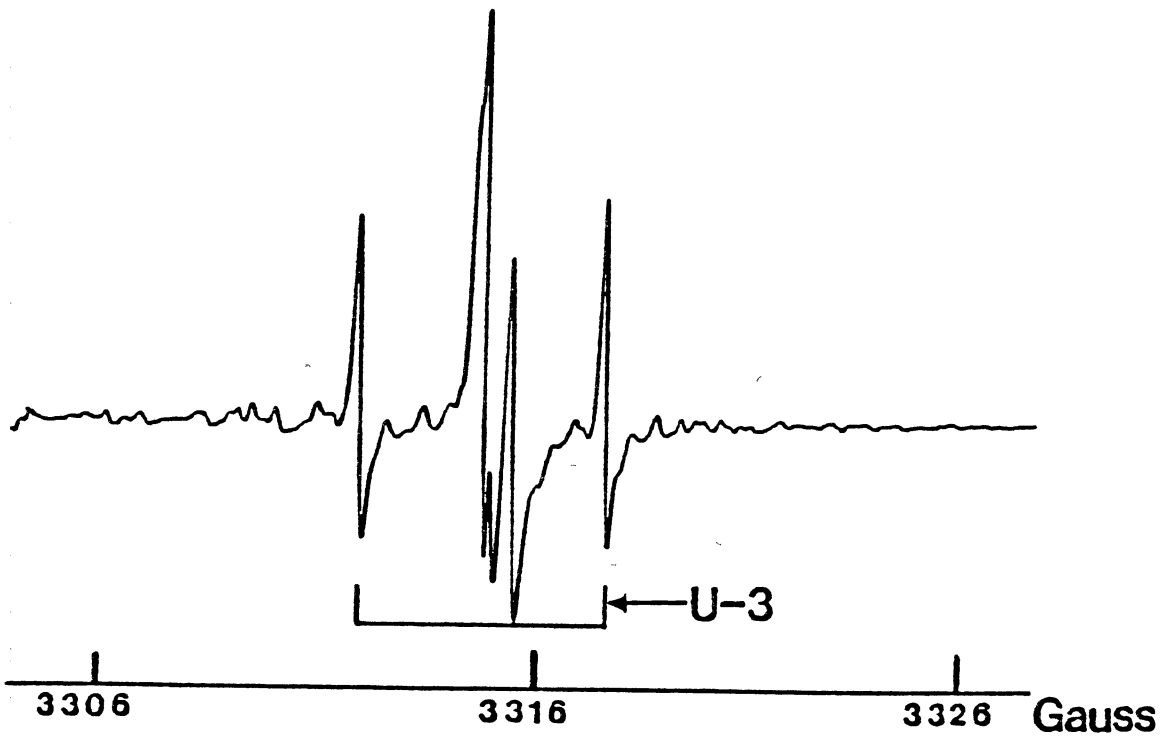

Figure 23. EPR spectrum for U-3 center after the U-2 center disappeared at 137 K. The microwave frequency is 9.281504 GHz

lines while the low-field line splits into two separate lines with one line being doubly degenerate. At each rotation interval, the magnetic field and microwave frequency for each line were recorded. The magnetic field values were obtained from a NMR Gaussmeter, which has a proton probe adjacent to the pole cap, and the frequencies were obtained from a frequency counter, which was connected to the microwave bridge. After completing the angular dependence for the U-3 center, field correction values were measured using a standard $MgO:Cr^{3+}$ sample that has a g value of 1.9799.

The field correction consisted of measuring the standard $MgO:Cr^{3+}$ sample while using the same conditions used for the quartz sample (i.e., position and temperature). Magnetic field values and frequencies were recorded, at each 5^{o} interval, for the large Cr^{3+} line centered approximately on 3355 G.

Knowing the g value of the standard sample and using the recorded frequencies for each line, new magnetic field values were calculated. This, in turn, was subtracted from the recorded magnetic field values of the $MgO:Cr^{3+}$ sample. This subtraction gives the magnetic field difference between the position of the proton probe (i.e., pole cap) and the position of the sample. The difference was then used to correct the magnetic field values previously obtained form the U-3 angular measurements. Table II provides the angles, uncorrected field values, corrected field values, calculated

TABLE II

ANGULAR DEPENDENT DATA FOR U-3 CENTERS AT 77K

ANGLE	UNCORRECTED FIELD (GAUSS)	CORRECTED FIELD (GAUSS)	CALCULATED FIELD (GAUSS)	MICROWAVE FREQUENCY (MHz)
+70	3317.456	3316.774	3316.450	9294.983
	3317.456	3316.774	3316.514	9294.983
	3320.169	3319.487	3319.169	9294.958
	3323.547	3322.865	3322.558	9294.954
	3324.703	3324.022	3323.688	9294.895
	3326.592	3325.911	3325.576	9294.984
+65	3317.443	3316.683	3316.428	9294.889
	3317.443	3316.683	3316.460	9294.889
	3320.305	3319.545	3319.250	9294.883
	3323.563	3322.803	3322.554	9295.021
	3324.800	3324.041	3323.771	9294.995
	3326.307	3325.548	3325.264	9294.884
+60	3317.479	3316.639	3316.416	9294.921
	3317.479	3316.639	3316.424	9294.921
	3320.336	3319.495*	3319.291	9295.007
	3323.627	3322.787	3322.558	9294.949
	3324.928	3324.088	3323.832	9294.961
	3326.013	3325.172	3324.942	9294.976
+55	3317.475	3316.657	3316.407	9294.887
	3317.475	3316.657	3316.417	9294.887
	3320.310	3319.492	3319.290	9294.865
	3323.648	3322.830	3322.570	9294.832
	3324.948	3324.130	3323.870	9294.893
	3325.698	3324.879	3324.617	9294.861
+50	3317.521	3316.726	3316.410	9294.837
	3317.521	3316.726	3316.431	9294.837
	3320.322	3319.527	3319.246	9294.945
	3323.701	3322.906	3322.588	9294.787
	3324.953	3324.158	3323.883	9294.836
	3325.394	3324.600	3324.299	9294.806
+45	3317.590	3316.737*	3316.434	9295.017
	3317.590	3316.737*	3316.461	9295.017
	3320.312	3319.459	3319.161	9294.978
	3323.744	3322.891*	3322.613	9294.903
	3325.089	3324.236	3323.872	9294.919
	3325.089	3324.236	3323.996	9294.919
+40	3317.624	3316.836	3316.477	9294.854

TABLE II (continued)

ANGLE (DEGREE)	UNCORRECTED FIELD (GAUSS)	CORRECTED FIELD (GAUSS)	CALCULATED FIELD (GAUSS)	MICROWAVE FREQUENCY (MHz)
	3317.624	3316.836	3316.506	9294.854
	3320.277	3319.489	3319.037	9294.921
	3323.818	3323.030	3322.644	9294.848
	3324.948	3324.160	3323.715	9294.836
	3324.948	3324.160	3323.836	9294.836
+35	3317.847	3317.021	3316.539	9295.197
	3317.847	3317.021	3316.567	9295.197
	3320.158	3319.332	3318.879	9295.241
	3324.000	3323.174*	3322.679	9295.310
	3324.718	3323.892	3323.463	9295.295
	3325.098	3324.272	3323.777	9295.275
+30	3317.912	3317.144	3316.617	9295.244
	3317.912	3317.144	3316.642	9295.244
	3319.931	3319.163	3318.690	9295.221
	3324.006	3323.238	3322.718	9295.254
	3324.504	3323.736	3323.246	9295.232
	3324.999	3324.231	3323.697	9295.233
+25	3318.003	3317.152	3316.710	9295.169
	3318.003	3317.152	3316.731	9295.169
	3319.722	3318.871	3318.476	9295.133
	3324.012	3323.161*	3322.758	9295.263
	3324.324	3323.473	3323.072	9295.316
	3324.889	3324.038	3323.599	9295.203
+20	3318.094	3317.271	3316.814	9295.216
	3318.094	3317.271	3316.831	9295.216
	3319.500	3318.677	3318.244	9295.247
	3324.177	3323.354	3322.799	9295.237
	3324.177	3323.354	3322.944	9295.237
	3324.770	3323.947	3323.485	9295.228
+15	3318.183	3317.372	3316.927	9295.098
	3318.183	3317.372	3316.939	9295.098
	3319.219	3318.408	3318.001	9295.147
	3324.091	3323.280	3322.840	9295.142
	3324.091	3323.280	3322.866	9295.142
	3324.610	3323.799	3323.359	9295.218
+10	3318.274	3317.501	3317.045	9295.203
	3318.274	3317.501	3317.053	9295.203
	3318.989	3318.216	3317.754	9295.124
	3324.085	3323.313	3322.840	9295.133
	3324.085	3323.313	3322.879	9295.133

TABLE II (continued)

ANGLE (DEGREE)	UNCORRECTED FIELD (GAUSS)	CORRECTED FIELD (GAUSS)	CALCULATED FIELD (GAUSS)	MICROWAVE FREQUENCY (MHz)
	3324.465	3323.692	3323.225	9295.135
+5	3318.396	3317.593	3317.163	9295.151
	3318.396	3317.593	3317.167	9295.151
	3318.720	3317.916	3317.511	9295.259
	3324.204	3323.400	3322.868	9295.157
	3324.204	3323.400	3322.915	9295.157
	3324.204	3323.400	3323.087	9295.157
0	3318.494	3317.680	3317.279	9295.292
	3324.166	3323.353	3322.949	9295.256
-5	3317.759	3317.047	3317.067	9293.915
	3318.024	3317.312	3317.386	9293.932
	3318.024	3317.312	3317.389	9293.932
	3323.654	3322.942*	3322.814	9293.903
	3323.654	3322.942	3322.978	9293.903
	3323.654	3322.942	3323.079	9293.903
-10	3317.566	3316.837	3316.879	9293.955
	3318.145	3317.417	3317.484	9293.931
	3318.145	3317.417	3317.488	9293.931
	3323.347	3322.618	3322.686	9293.942
	3323.794	3323.065*	3323.002	9293.963
	3323.794	3323.065	3323.256	9293.963
-15	3317.442	3316.703	3316.724	9293.940
	3318.246	3317.506	3317.571	9293.897
	3318.246	3317.506	3317.575	9293.897
	3323.255	3322.516	3322.570	9293.914
	3323.682	3322.943*	3323.020	9293.950
	3324.131	3323.392	3323.474	9293.944
-20	3317.326	3316.584	3316.604	9293.915
	3318.325	3317.584	3317.643	9293.946
	3318.325	3317.584	3317.646	9293.946
	3323.155	3322.414	3322.467	9293.947
	3323.719	3322.977	3323.032	9293.905
	3324.403	3323.662	3323.725	9293.942
-25	3317.228	3316.463	3316.525	9293.900
	3318.387	3317.622	3317.699	9293.930
	3318.387	3317.622	3317.700	9293.930
	3323.113	3322.348	3322.383	9293.919
	3323.742	3322.978	3323.038	9293.917
	3324.671	3323.907	3324.002	9293.919

TABLE II (continued)

ANGLE (DEGREE)	UNCORRECTED FIELD (GAUSS)	CORRECTED FIELD (GAUSS)	CALCULATED FIELD (GAUSS)	MICROWAVE FREQUENCY (MHz)
-30	3317.179	3316.433	3316.488	9293.917
	3318.431	3317.686	3317.733	9293.952
	3318.431	3317.686	3317.738	9293.952
	3323.012	3322.266	3322.318	9293.943
	3323.737	3322.991	3323.036	9293.917
	3324.990	3324.244	3324.297	9293.911
-35	3317.175	3316.449	3316.494	9293.917
	3318.456	3317.730	3317.746	9293.937
	3318.456	3317.730	3317.757	9293.937
	3322.993	3322.267	3322.276	9293.977
	3323.729	3323.003	3323.028	9293.955
	3325.292	3324.566	3324.602	9293.928
-40	3317.204	3316.505	3316.542	9293.899
	3318.452	3317.754	3317.739	9293.950
	3318.452	3317.754	3317.756	9293.950
	3322.979	3322.280	3322.258	9293.941
	3323.715	3323.016	3323.013	9293.974
	3325.607	3324.909	3324.907	9293.990
-45	3317.362	3316.660	3316.632	9294.024
	3318.480	3317.778	3317.712	9294.058
	3318.480	3317.778	3317.732	9294.058
	3323.010	3322.308	3322.264	9294.074
	3323.744	3323.043	3322.991	9294.074
	3325.942	3325.240	3325.204	9294.067
-50	3317.487	3316.808	3316.759	9293.998
	3318.416	3317.736	3317.666	9293.992
	3318.416	3317.736	3317.687	9293.992
	3323.025	3322.346	3322.296	9293.947
	3323.705	3323.026	3322.964	9293.983
	3326.193	3325.514	3325.486	9293.985
-55	3317.602	3316.929	3316.920	9293.966
	3318.364	3317.691	3317.602	9294.032
	3318.364	3317.691	3317.619	9294.032
	3323.081	3322.408	3322.352	9293.968
	3323.651	3322.977	3322.931	9294.007
	3326.447	3325.773	3325.746	9293.985
-60	3317.746	3317.056	3317.111	9293.982
	3318.272	3317.582	3317.522	9293.925
	3318.272	3317.582	3317.529	9293.925
	3323.118	3322.428	3322.430	9293.979

TABLE II (continued)

ANGLE (DEGREE)	UNCORRECTED FIELD (GAUSS)	CORRECTED FIELD (GAUSS)	CALCULATED FIELD (GAUSS)	MICROWAVE FREQUENCY (MHz)
	3323.625	3322.936	3322.894	9293.992
	3326.712	3326.022	3325.977	9293.977
-65	3318.142	3317.433	3317.324	9294.016
	3318.142	3317.433	3317.418	9294.016
	3318.142	3317.433	3317.430	9294.016
	3323.197	3322.487	3322.528	9293.967
	3323.570	3322.861	3322.853	9293.992
	3326.939	3326.230	3326.174	9293.976

* not used in line fitting program

field values (from the line position program), and microwave frequencies for the angular dependence study of the U-3 center. Table III shows the field correction factors determined from the standard MgO:Cr^{3+} sample. Table IV gives the parameters calculated (from the line fitting program) for the g and A tensors and Table V gives the principal directions for each tensor. Figure 24 shows a plot of the magnetic field versus the angle for the computer predicted dependence. This also shows pairs of high-field and low-filed lines that were selected to give the "best" fit.

Discussion

The goal of this experiment was to develop an appropriate model for the U-3 center. Chen [28] suggested a model that contained an electron localized on a silicon and with a proton forming an OH^- molecule on a nearby oxygen. His suggestion was based on various observations; however, some of the observations do not coincide with mine. A detailed description of observations and suggested model for the U-3 center is given in Chapter 1.

One of the differences is that the production curves do saturate with high doses of radiation (less than 100 Mrads). The U-2 and U-3 centers saturate at 20 minutes of irradiation while the U-4 center continues to grow. Another difference includes differing parameter values for the g and A tensors and, thus, differing principal directions.

TABLE III

FIELD-CORRECTION FACTORS AS DETERMINED FROM STANDARD MgO:Cr^{3+} SAMPLE FOR U-3 CENTERS AT 77K

ANGLE (DEGREE)	H Cr^{3+} (GAUSS)	MICROWAVE FREQUENCY (MHz)	DELTA H (GAUSS)
+70	3355.488	9292.639	0.68165
+65	3355.528	9292.533	0.75912
+60	3355.601	9292.510	0.84042
+55	3355.627	9292.646	0.81793
+50	3355.666	9292.819	0.79467
+45	3355.665	9292.652	0.85316
+40	3355.647	9292.784	0.78791
+35	3355.648	9292.681	0.82609
+30	3355.639	9292.817	0.76779
+25	3355.646	9292.607	0.85101
+20	3355.632	9292.645	0.82329
+15	3355.634	9292.684	0.81141
+10	3355.620	9292.752	0.77286
+05	3355.643	9292.731	0.80324
00	3355.628	9292.662	0.81315
-05	3356.106	9294.264	0.71220
-10	3356.114	9294.241	0.72850
-15	3356.115	9294.215	0.73948
-20	3356.111	9294.198	0.74143
-25	3356.120	9294.159	0.76451
-30	3356.101	9294.158	0.74587
-35	3356.076	9294.143	0.72608
-40	3356.040	9294.121	0.69862
-45	3356.050	9294.140	0.70156
-50	3356.018	9294.114	0.67915
-55	3356.018	9294.129	0.67334
-60	3356.029	9294.113	0.68971
-65	3356.023	9294.043	0.70918

TABLE IV

SPIN-HAMILTONIAN PARAMETERS FOR THE U-3 CENTER

	X	Y	Z	Theta	Phi	Psi
g	1.998821	2.000636	1.99997	130.52	43.25	-32.27
A	-16.29	-28.81	-10.42	104.91	96.71	89.33

TABLE V

PRINCIPAL DIRECTION FOR EACH TENSOR

	g_x	g_y	g_z	A_x	A_y	A_z
Theta	113.95°	50.00°	130.52°	14.92°	89.35°	104.91°
Phi	65.56°	-2.57°	46.75°	9.31°	-83.12°	6.71°

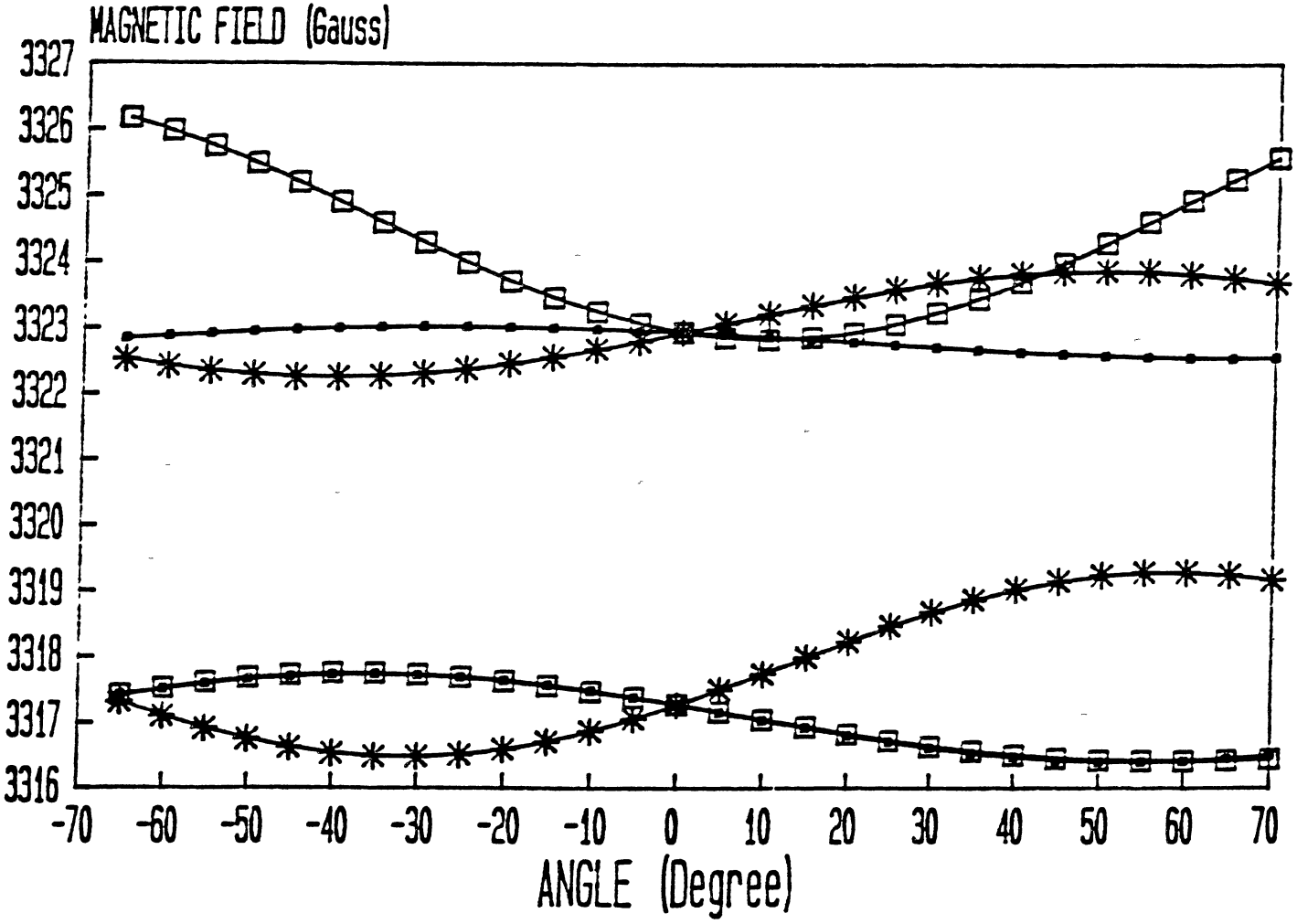

Figure 24. Computer predicted angular dependence of the U-3 center at 77 K

However, these new observations do not warrant a change in the proposed model.

CHAPTER VII

EXPERIMENTAL METHOD AND RESULTS FOR THE U-5 CENTER

Defect Production and Thermal Anneal

This experiment is a continuation of the defect production described in the previous chapter. Basically, this work entails a long term irradiation of an unswept EPR size quartz sample at 77 K. The irradiation was performed using 1.75-MeV electrons for up to 4 hours. A detailed description of the defect production is given in Chapter 3.

EPR data were taken for selected irradiation times in the "in-phase" and "out-of-phase" conditions. Figure 25 shows the c-axis EPR spectra at 12 minutes of irradiation in both phase conditions. The "in-phase" condition exhibits the U-1 center and aluminum hole. These defects were previously reported by Markes and Halliburton [29]. The "out-of-phase" condition exhibits the U-2, U-3, and U-4 centers which were also reported by Markes and Halliburton [29].

Figure 26 shows the "in-phase" EPR data at 12 minutes and 4 hours of irradiation. There is a sizeable defect which grew in that has a characteristic hyperfine doublet split by 41.1 G with each line having a width of 2.5 G.

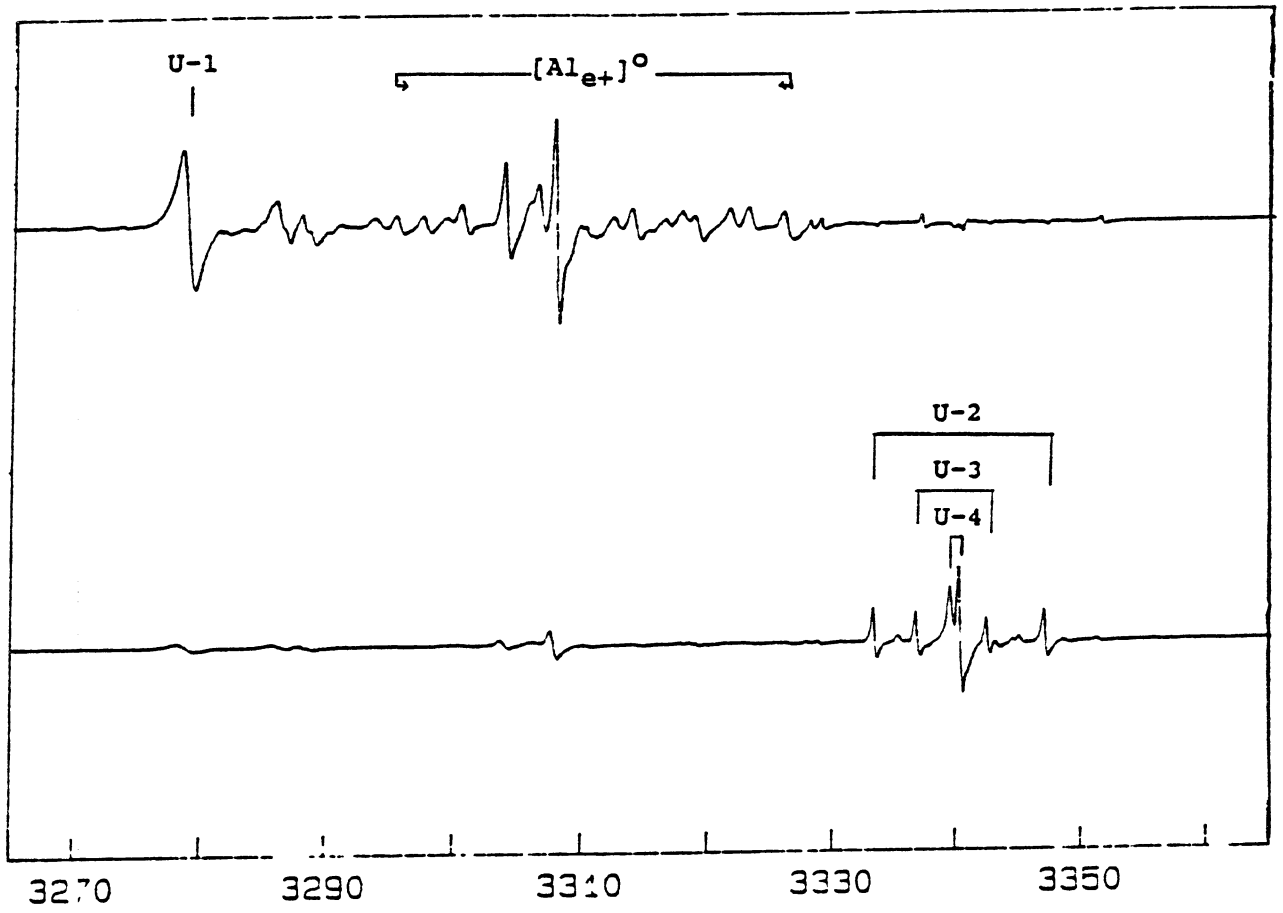

Figure 25. EPR spectra showing the "in-phase" (top) and "out-of-phase" (bottom) conditions after a 12 minute 77 K irradiation. Data taken at 77 K along the c-axis

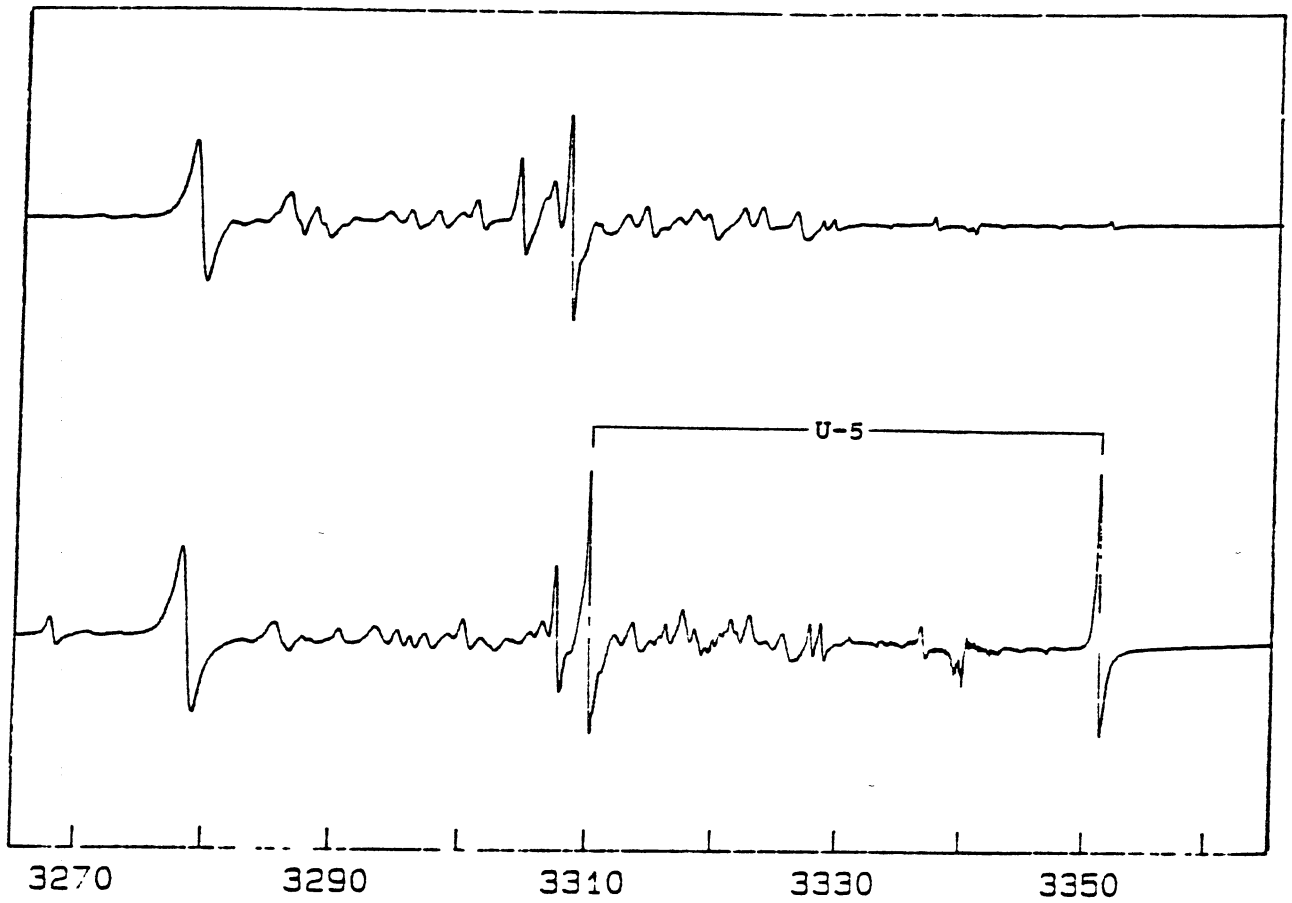

Figure 26. "in-phase" EPR spectra at 12 minutes of irradiation (top) and 4 hours of irradiation (bottom). Data taken at 77 K along the c-axis

This new defect is noted as the U-5 center, U meaning unknown. Figure 27 shows the intensity of the defect plotted as a function of irradiation time. This exhibits an unsaturated defect concentration that grows nearly linear with dose.

The "out-of-phase" condition at 12 minutes and 4 hours of irradiation is shown in figure 28. This shows defects that grew in after the U-2 and U-3 centers had been saturated. These new defects saturate when they meet the U-2 and U-3 centers concentration level.

The thermal anneal for the U-5 center is shown in figure 29. The defect anneal is nearly linear and anneals out at 125 K which is the area where the H^{o} (hydrogen atom) anneals. This anneal verifies the defects' stability only at low temperatures.

Discussion

The purpose of this experiment was to report defects, if any, that are produced from long term 77 K irradiations. The U-5 center was produced, thus supporting a successful experiment.

The U-5 center is suggested to be a hydrogen-related center because it exhibits a doublet nature due to a hyperfine interaction with a 100% abundant I = 1/2 nucleus. Furthermore, it anneals out in the same area as the hydrogen atom.

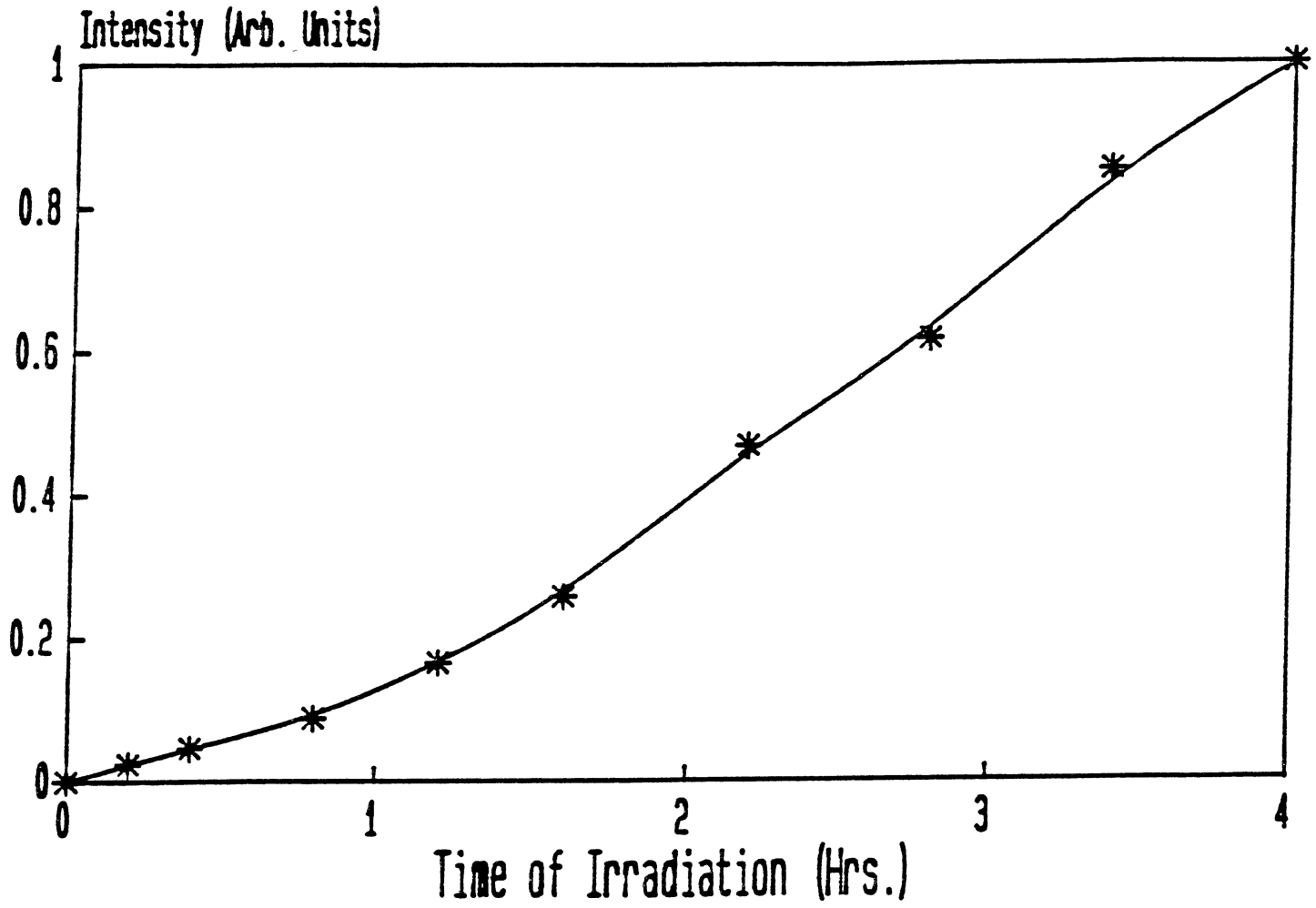

Figure 27. Defect production of the U-5 center as a function of irradiation time

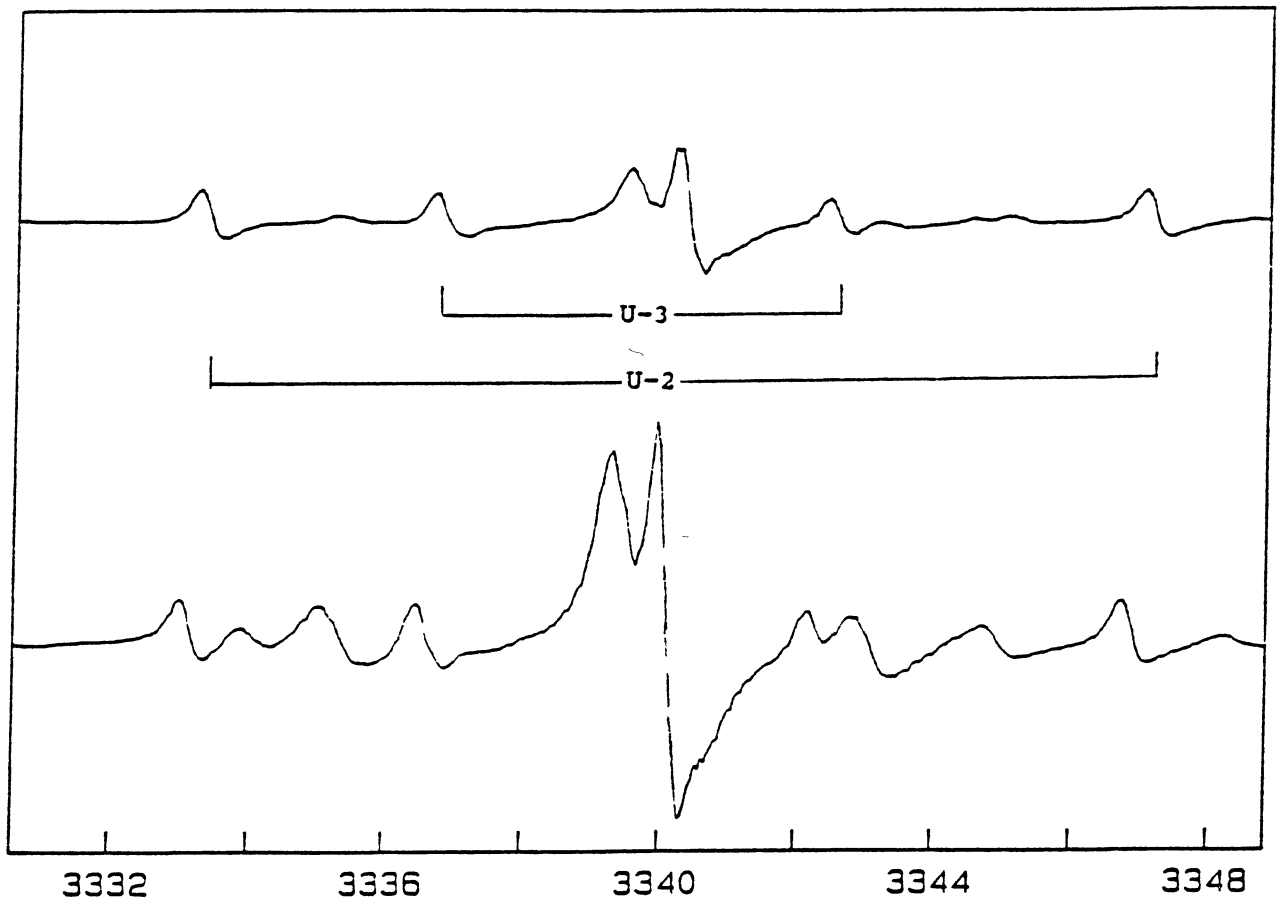

Figure 28. "out-of-phase" EPR spectra at 12 minutes of irradiation (top) and 4 hours of irradiation (bottom). Data taken at 77 K along the c-axis

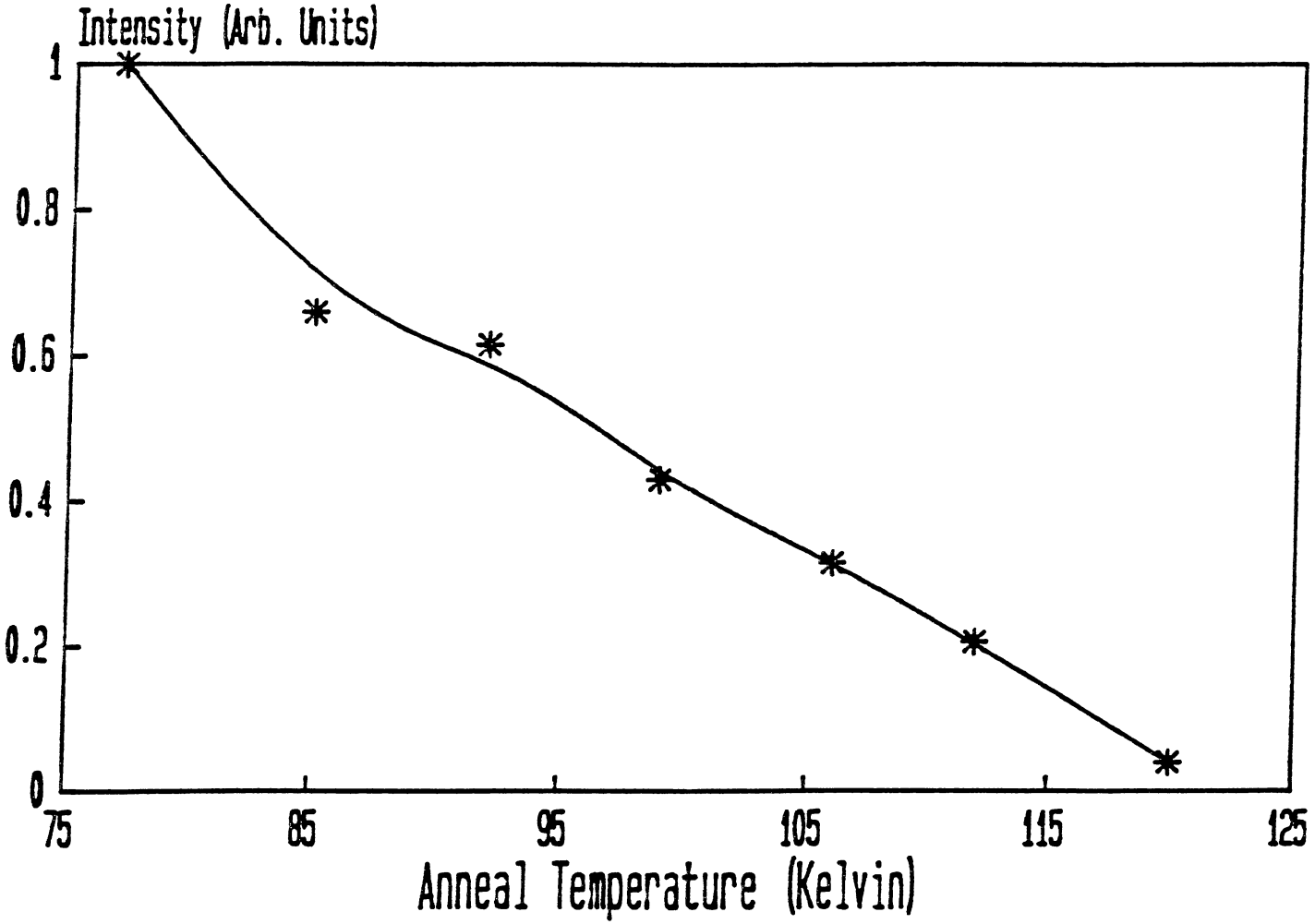

Figure 29. Thermal anneal of the U-5 center

The 500 G split doublet, that is characteristic for the hydrogen atom, shows a strong hyperfine interaction. The 41 G split doublet for the U-5 center gives an intermediate hyperfine interaction and the 5.7 G split doublet for the U-3 center gives a weak hyperfine interaction. Taking these interactions into consideration and doing an in-depth angular dependence study can lead to a possible model for the U-5 center. Other experiments, such as ENDOR and spin-lattice relaxations, can help form a concrete model for this defect.

A SELECTED BIBLIOGRAPHY

1. Halliburton, L. E., Cryst. Latt. Def. 12, 163 (1985).

2. Armington, A. F., A. Kahan and F. K. Euler, ETS Technical Memorandum No. 3, Solid State Division, Deputy for Electronic Technology, RADC, Hascoin, AFB, Mass. 01731, September 1976.

3. Halliburton, L. E., J. J. Martin, and D. R. Koehler, in Precision Frequency Control, (Academic Press, New York, 1985), Vol. 1, Chapter 1.

4. Cady, W. G., Piezoelectricity, Vols. I and II (Dover Publications, New York, 1964).

5. King, J. C., Bell Syst. Tech. J. 38, 573 (1959).

6. Weil, J. A., Phys. Chem. Miner. 10, 149 (1984).

7. Martin, J. J., J. Appl. Phys. 56, 2536 (1984).

8. Nowick, A. S., and M. W. Stanley, J. Appl. Phys. 40, 4995 (1969).

9. Stevels, J. M., and J. Volger, Philips Res. Rep. 17, 283 (1969).

10. Nuttal, R. H. D., and J. A. Weil, Can. J. Phys. 59, 1709 (1981).

11. Nuttal, R. H. D., and J. A. Weil, Can. J. Phys. 59, 1886 (1981).

12. Weeks, R. A., J. Appl. Phys. 27, 1376 (1956).

13. Weeks, R. A., and C. M. Nelson, J. Am. Ceram. Soc. 43, 399 (1960).

14. Silsbee, R. H., J. Appl. Phys. 32, 1459 (1961).

15. Feigl, F. J., W. B. Fowler, and K. L. Yip, Solid State Commun. 14, 225 (1974).

16. Yip, K. L., and W. B. Fowler, Phys. Rev. B 11, 2327 (1975).

17. Jani, M. G., MS Thesis, Oklahoma State University, (1979).

18. Rudra, J. K., W. B. Fowler, and F. J. Feigl, Phys. Rev. Lett. 55, 2614 (1985).

19. Halliburton, L. E., B. D. Perlson, R. A. Weeks, J. A. Weil, and M. C. Wintersgill, Solid State Commun. 30, 575 (1975).

20. Isoya, J., J. A. Weil, and L. E. Halliburton, J. Chem. Phys. 74, 10 (1981).

21. Weeks, R. A. and M. M. Abraham, Bull. Am. Phys. Soc. 10, 374 (1965).

22. Bossoli, R. B., M. G. Jani, and L. E. Halliburton, Solid State Commun. 44, 213 (1982).

23. Jani, M. G., Ph.D. Dissertation, Oklahoma State University, (1982).

24. Weeks, R. A. and M. M. Abraham, J. Chem. Phys. 42, 68 (1965).

25. Perlson, B. D. and J. A. Weil, J. Magn. Res. 15, 594 (1974).

26. Isoya, J., J. A. Weil, and P. H. Davis, J. Phys. Chem. Solids 44, 335 (1983).

27. Nuttal, R. H. D. and J. A. Weil, Solid State Commun. 33, 99 (1980).

28. Chen, C. Y., Ph.D. Dissertation, Oklahoma State University, (1985).

29. Markes, M. E. and L. E. Halliburton, J. Appl. Phys. 50, 8172 (1979).

30. Jani, M. G., L. E. Halliburton, and A. Halperin, Phys. Rev. Lett. 56, 1392 (1986).

31. ER Series User's Manual, (IBM Instruments, Inc., Dept. 74P, P.O. Box 332, Danbury, CT 06810, 1982).

32. Mitchell, E. W. J. and E. G. S. Paige, Proc. Phys. Soc. (London) B67, 262 (1954).

33. Mitchell, E. W. J. and E. G. S. Paige, Phil. Mag. 1, 1085 (1956).

34. Arnold, G. W., Phys. Rev. A 139, 1234 (1965).

35. Arnold, G. W., Phys. Rev. A 140, 176 (1965).

VITA

Benjamin Mark Zapata

Candidate for the Degree of

Master of Science

Thesis: ELECTRON PARAMAGNETIC RESONANCE AND OPTICAL STUDIES OF CRYSTALLINE SILICON DIOXIDE

Major Field: Physics

Biographical:

Personal Data: Born in San Antonio, Texas, December 22, 1961, the son of Manuel and Stephanie Louise Zapata.

Education: Graduated from O. W. Holmes High School, San Antonio, Texas, in 1979, received Bachelor of Science Degree in 1987 from The University of Texas at San Antonio, San Antonio, Texas; completed the requirements for the Degree of Master of Science at Oklahoma State University, Stillwater, Oklahoma, in December, 1990.